TECHNISCHE
UNIVERSITÄT
WIEN
Vienna | Austria

Diplomarbeit

Nernst- and Seebeck effect at high temperatures and high magnetic fields

zur Erlangung des akademischen Grades

Diplom-Ingenieur/in

im Rahmen des Studiums

Technische Physik

unter der Leitung von

Univ.Prof. Dipl.-Ing. Dr.techn. Ernst Bauer
Projektass. Dipl. Ing Michael Parzer

ausgeführt am Institut für Festkörperphysik
der Technischen Universität Wien

eingereicht von

Tobias Schmid, BSc
Matrikelnummer: 01326342

Wien, 14.08.2022   _____   _____
                    (Unterschrift Verfasser/in)   (Unterschrift Betreuer/in)

Zusammenfassung

Im Rahmen dieser Diplomarbeit wurde ein Messaufbau zur Untersuchung des Nernst-
und Seebeck-Effekts bei hohen Temperaturen und hohen Magnetfeldern entworfen
und realisiert. Der Messaufbau erlaubt gleichzeitige Messungen beider Effekte für
Temperaturen bis 560 Kelvin und Magnetfeldern bis 10 Tesla. Neben der experi-
mentellen Arbeit werden die theoretischen Grundlagen beider Effekte präsentiert.
Ausgehend davon werden Messgleichungen abgeleitet, die konstante Störspannun-
gen und systematische Fehler des Messaufbaus kompensieren. Zur Automatisierung
des Messprozesses wurde eine Messsoftware sowie eine grafische Benutzeroberfläche
entwickelt. Der Messaufbau wurde für eine Vielzahl verschiedener polykristalline
Materialien, für die verlässliche Referenzdaten publiziert wurden, getestet und op-
timiert. Für sämtliche Referenzproben konnten die publizierten Messergebnisse re-
produziert werden, was den Einsatz des Messaufbaus für zukünftige Forschung am
Institut rechtfertigt.

Abstract

As part of this diploma thesis a measurement setup to study the Seebeck- and Nernst effect at high temperatures and high magnetic fields was designed and created. The measurement setup allows for simultaneous measurements of both effects for temperatures up to 560 Kelvin and magnetic fields up to 10 Tesla. Apart from the experimental work, the underlying theory of both effects is presented. Based on the theoretical concepts, measurement equations are derived, that counteract constant spurious offset voltages and systematic errors of the measurement setup. For automation of the measurement process, a measurement software and a graphical user interface were developed. The measurement setup was tested and optimized using a wide variety of polycrystalline materials for which reliable reference data were published. For all reference samples the published results could be reproduced for both the Seebeck- and Nernst effect, allowing the measurement setup to be a reliable system for future research at the institute.

Contents

List of Figures

1 Introduction

Ever since their discovery, the thermoelectric effects, in particular the Seebeck effect, have continuously sparked attention and interest among scientists for basic research as well as technological applications. In presence of a magnetic field, thermomagnetic effects appear, with the Hall effect as their best known representative. Its thermoelectric analogue, the Nernst effect, has recently gained a lot of attention due to an additional contribution called the anomalous Nernst effect that was discovered in several different materials, primarily ferromagnets. A recent study outlined several advantages of energy harvesting materials based on this effect compared to those that are based on the Seebeck effect [1]. To test theoretical forecasts of promising materials reliable and precise measurements of thermoelectric effects are indispensable. While building an experimental setup for measurements of the Seebeck effect is simple and even compact commercial solutions exist, measurements of the Nernst effect are more challenging, mainly due to lower signals on average and the requirement of a controllable magnetic field that can reach reasonably high values.

This work documents the process of building and testing a measurement setup at TU Wien that can perform simultaneous Seebeck- and Nernst effect measurements at high temperatures and high magnetic fields. The goal is to confirm reference data of both effects for various materials using polycrystalline bulk samples synthesized at TU Wien. Additionally, it is aimed that the measurement setup is easy and practical to use by designing a measurement software, controlling and monitoring measurements accompanied by a graphical user interface.

For a brief theoretical introduction both the Seebeck- and Nernst effect are introduced from a phenomenological point of view, followed by a more precise semiclassical mathematical derivation using Boltzmann's transport equation. Using phenomenological expressions for both effects, a model setup is created. Based on this model, the measurement setup and the measurement software was designed and built. Following a description of the sample synthesis and preparation process the measurement results are presented and discussed for each individual sample. Afterwards the results are summarized, interpreted and future prospects for the measurement setup are discussed.

2 Theory

This chapter aims at providing a brief theoretical introduction into thermoelectricity, focusing on the Seebeck- and the Nernst effect. At first phenomenological explanations and expressions for both effects are given, followed by a compact semiclassical derivation of the transport coefficients for both effects.

2.1 Seebeck effect

In 1821, studying a circuit of a given material A that is connected with two wires of of material B Thomas Johann Seebeck observed a voltage that occurs solely based on the temperature difference of the contact points of material A and B [2].
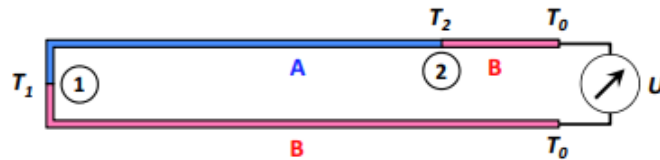
Figure 1: Circuit for the discovery of the Seebeck effect [3]. T_0, T_1, T_2 correspond to the temperature at the respective points in the circuit, while A and B stand for different material types. U represents the occurring voltage.
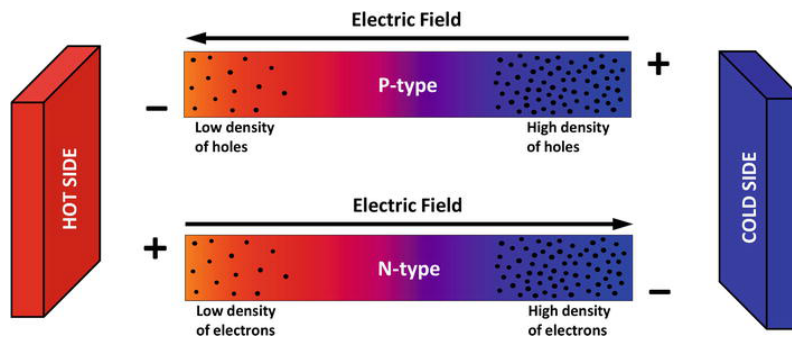
Figure 2: Schematic diagram of the microscopic process that leads to the occurrence of the Seebeck effect [2]. In semiconductors the type of mobile charge carriers (negatively charged electrons or positively charged electron holes) determine the direction of the resulting electric field.

Microscopically, a simplified classical explanation for the occurrence of this effect can be given by looking at a conductor where no external electrical current is present. Assuming both ends of a bar shaped conductor to be at different temperatures, mobile charge carriers at the higher temperature end will generally have higher velocities than those at lower temperature end resulting in a net velocity, pointing towards the end of lower temperature. This velocity generates charge carrier displacement, which results in an electrical field along the conductor [2]. Using the Seebeck coefficient S the relation between the resulting electric field and temperature gradient is

$$\vec{E} = -S\nabla T. \tag{1}$$

As shown in Figure 2, the direction of the electric field is connected to the sign of the mobile charge carriers. For p-type semiconductors, where only electron holes are mobile charge carriers, S is always positive, while for n-type semiconductors containing only electrons as mobile charge carriers, S is always negative. For general conductors where both types of mobile charge carriers are present, the sign of S can give an indication on which of the charge carriers are dominant [2].

Using an experimental circuit, as shown in Figure 1, an occurring voltage as a result of the Seebeck effect can be expressed as

$$U_{AB} = \int_{T_1}^{T_2} [S_A(T) - S_B(T)] dT, \tag{2}$$

where $S_A(T)$ and $S_B(T)$ are the Seebeck coefficients of the respective materials A and B. They are most commonly given in $\mu V/K$. For the Seebeck effect, the observed voltage always corresponds to the direction along which the temperature gradient occurs. For example: For a temperature gradient in the y direction and small temperature differences, equation (1) can be approximated as

$$U_{AB} = U_y = [S_A(\overline{T}) - S_B(\overline{T})] \Delta T_y, \tag{3}$$

using $\overline{T} = \frac{T_1 + T_2}{2}$ and $\Delta T_y = T_2 - T_1$.

Applying a magnetic field transverse to the temperature gradient can lead to a change in the Seebeck coefficient, which is usually referred to as magneto-Seebeck effect. In general, the magneto-Seebeck effect is always accompanied by the Nernst effect [4]. Since the dependence of the Seebeck coefficient on both temperature and transversal magnetic field is studied in this diploma thesis, all given Seebeck coefficients will further be discussed as functions of both quantities but will be written without their dependencies.

2.2 Nernst effect

In 1886 Walter Nernst and Andreas Ettinghausen discovered the following phe-
nomenon: When a temperature gradient and a magnetic field, which are perpendic-
ular to each other, are applied to a conducting material, an electromotive force is
induced normal to both quantities, and a voltage can be observed in this direction
[5, 6]. The effect was originally named Nernst-Ettinghausen effect, although today
it is more commonly only referred to as Nernst effect. Microscopically, the Nernst
effect occurs due to the Lorentz force acting on the charge carries that are displaced
by the temperature gradient. By nature of the Lorentz force, it deflects both types of
charge carriers in opposite directions. Consequently, both contribute to the Nernst
effect [7]. Often misunderstood, the Nernst effect is an intrinsic effect and does not
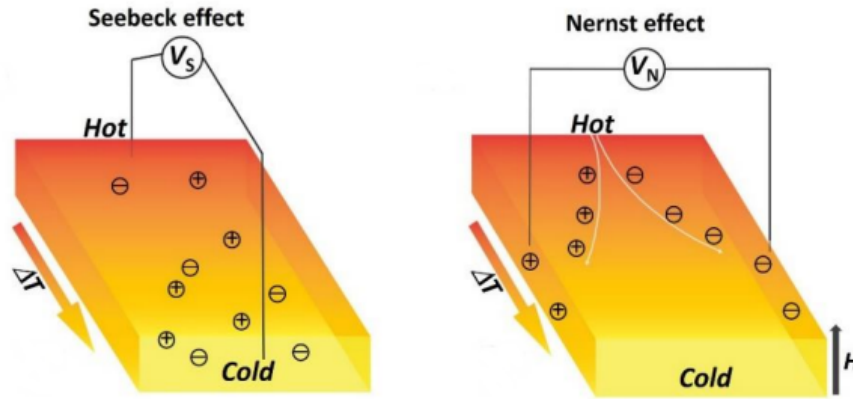
Figure 3: Schematic diagram for comparison of the Seebeck- and Nernst effect [7]. ΔT indicates
the direction of the temperature gradient while H shows the direction of the magnetic field. V_s
and V_N are the voltages occurring due to the Seebeck- and Nernst effect respectively.

require external currents or a circuit with load resistance to occur. In addition, if
the material has a spontaneous magnetization, an additional voltage contribution
becomes superimposed on the signal. This term is usually called the anomalous
Nernst effect (ANE). In a more general theoretical picture, the anomalous Nernst
effect is geometrically connected to the Berry curvature of the conduction electrons
near the Fermi energy [8]. Recently a significant magnitude of the effect was also
discovered in a chiral antiferromagnet [9]. A detailed analysis of the anomalous
Nernst effect and related phenomena can be found in [10]. For ferromagnetic mate-
rials an observable electric field as a result of these effects can phenomenologically
be described as [1]

$$\vec{E} = \vec{E}_{\text{Normal}} + \vec{E}_{\text{ANE}} = N_{\text{Normal}}(\vec{H} \times \nabla T) + N_{\text{ANE}}(\mu_0 \vec{M} \times \nabla T), \tag{4}$$

where N_{Normal} and N_{ANE} are referred to as Nernst coefficient and anomalous Nernst
coefficient of a given material. Their unit is µV/KT, although more commonly the

product of the coefficient with the magnetic field is given, as it has the same unit as the Seebeck coefficient. In this form it is often called Nernst signal and can be written in compact form as

$$N_{\text{Signal}} = N H_z = \frac{E_x}{\nabla_y T},$$ (5)

using $N = N(T, \vec{H}, \vec{M}) = N_{\text{Normal}} + \chi N_{\text{ANE}}$ and $\vec{M} = \chi \vec{H}$.
Approximating the voltage U_x as

$$U_x = \int_{x_1}^{x_2} E_x(x) \cdot dx \approx E \cdot \Delta x$$ (6)

and approximating the temperature gradient along the y direction as

$$\nabla_y T \approx \frac{\Delta T_y}{\Delta y}$$ (7)

an expression for a measurable voltage yields

$$U_x = N H_z \Delta T_y \frac{\Delta x}{\Delta y}.$$ (8)

Analogous to the Seebeck coefficient all Nernst coefficients will from now on be written without their functional dependencies.

2.3 Semiclassical derivation of transport coefficients

A simple and common approach to derive theoretical expressions for transport coefficients such as the Seebeck- and Nernst coefficients is to use Boltzmann's equation [3]. The equation is used to describe the change of the probability density function f of charge carriers in solids, assuming an impact of external forces, diffusion and collision. Further, assuming electrons as charge carriers with a well defined momentum $\vec{k}$, Boltzmann's equation yields:

$$\frac{\partial f(\vec{r},\vec{k},t)}{\partial t} = -\vec{v} \cdot \nabla_r f - \frac{e}{\hbar}(\vec{E} + \vec{v} \times \vec{B}) \cdot \nabla_{\vec{k}} f + \left(\frac{\partial f(\vec{r},\vec{k},t)}{\partial t}\right)_{Collision}. \tag{9}$$

Defining the electric charge current density $\vec{J}_q$ and heat current density $\vec{J}_h$ as

$$\vec{J}_q = \frac{1}{4\pi^3\hbar}\int e\vec{v}(\vec{k})f(\vec{k})d^3k, \tag{10}$$

$$\vec{J}_h = \frac{1}{4\pi^3\hbar}\int [E(\vec{k})-\mu]\nabla_{\vec{k}}E(\vec{k})f(\vec{k})d^3k \tag{11}$$

and using the well known approaches of linearisation and relaxation time approximation as well as $\vec{B} = 0$ for (7) yields:

$$\vec{J}_q = L^{11}\vec{E} + L^{12}\left(-\frac{\nabla T}{T}\right), \tag{12}$$

$$\vec{J}_h = L^{21}\vec{E} + L^{22}\left(-\frac{\nabla T}{T}\right). \tag{13}$$

With general transport coefficients L^{ij} that are defined as

$$\mathcal{L}^{(\alpha)} = \frac{e^2}{4\pi^3\hbar}\int\int dS_E dE \frac{\tau(\vec{k})\vec{v}_{\vec{k}}\vec{v}_{\vec{k}}[E(\vec{k}-\mu]^\alpha}{v(k)}\left(-\frac{\partial f_0}{\partial E}\right), \tag{14}$$

$$L^{11} = \mathcal{L}^{(0)}, \tag{15}$$

$$L^{21} = L^{12} = \frac{1}{e}\mathcal{L}^{(1)}, \tag{16}$$

$$L^{22} = \frac{1}{e^2}\mathcal{L}^{(2)}, \tag{17}$$

using the relaxation time τ and Fermi-Dirac distribution f_0.
The inetgral (12) can be solved by defining the tensor

$$\hat{\sigma}(E_f) = \frac{e^2}{4\pi^3\hbar}\int_{E(\vec{k})=const} dS_E \frac{\tau(\vec{k})\vec{v}_{\vec{k}}\vec{v}_{\vec{k}}}{v(k)} \tag{18}$$

and using the Sommerfeld expansion yielding

$$L^{11} = \hat{\sigma}(E_F), \tag{19}$$

$$L^{21} = L^{12} = \frac{\pi^2(k_B T)^2}{3e}\left(\frac{\partial\hat{\sigma}(E)}{\partial E}\right)|_{E=E_F}, \tag{20}$$

$$L^{22} = \frac{\pi^2(k_B T)^2}{3e}\hat{\sigma}(E_F). \tag{21}$$

Looking at equation (10) with $\nabla T = 0$ it becomes clear that $\hat{\sigma}(E_F)$ represents the conductivity tensor

$$\vec{J_q} = \hat{\sigma}(E_F)\vec{E}. \tag{22}$$

Using equation (10) again, but assuming a temperature gradient ($\nabla T \neq 0$) but no current ($\vec{J_q} = 0$) the equation describes the proportionality of electric field and temperature gradient.

$$\vec{E} = \frac{L^{12}}{L^{11}}\frac{\nabla T}{T} \tag{23}$$

Using equations (17) and (18) a general thermopower $\hat{S}$ in tensor form can be defined as

$$\hat{S} = \frac{L^{12}}{L^{11}T} = \frac{\pi^2(k_B T)^2}{3e\hat{\sigma}}\left(\frac{\partial\hat{\sigma}(E)}{\partial E}\right)|_{E=E_F}. \tag{24}$$

Equation (24) is most commonly known as Mott relation or Mott's formula often written using the thermoelectric conductivity tensor

$$\hat{\alpha} = \hat{S}\hat{\sigma} = \frac{\pi^2(k_B T)^2}{3e}\left(\frac{\partial\hat{\sigma}(E)}{\partial E}\right)|_{E=E_F}. \tag{25}$$

Using the heat conductivity tensor $\hat{\kappa}$ which can be derived in a similar way equations 10 and 11 yield

$$\vec{J_q} = \hat{\sigma}\vec{E} - \hat{\alpha}\nabla T, \tag{26}$$

$$\vec{J_h} = T\hat{\alpha}\vec{E} - \hat{\kappa}\nabla T. \tag{27}$$

Using equation 25 and setting $\vec{J_q} =$ the equation yields

$$\vec{E} = \frac{\hat{\alpha}}{\hat{\sigma}}\nabla T = \hat{S}\nabla T. \tag{28}$$

Comparing this result with the phenomenological equations of the previous sections it becomes clear that Seebeck coefficient and Nernst signal are linked to the transversal and longitudinal components of $\hat{S}$ respectively

$$S = \frac{E_x}{\nabla_x T} \equiv S_{xx} \equiv \frac{\alpha_{xx}}{\sigma_{xx}}, \tag{29}$$

$$N_{Signal} = \frac{E_x}{\nabla_y T} \equiv S_{xy} = \frac{\alpha_{xy}\sigma_{xx} - \sigma_{xx}\alpha_{xy}}{\sigma_{xx}^2 + \sigma_{xy}^2}. \tag{30}$$

Without the presence of a magnetic field $\vec{B}$ only the diagonal elements of $\hat{\sigma}$ and $\hat{\alpha}$ have a finite value. To obtain a finite Nernst signal and to understand the magnetic field dependence of the Seebeck effect, the Boltzmann equation needs to be discussed without the approximation of $\vec{B} = 0$. This is outlined in detail in Ref.[11] yielding modified longitudinal and transversal components of $\hat{\alpha}$ and $\hat{\sigma}$:

$$\sigma_0 = e^2 \int \tau(\vec{k})\vec{v}_{\vec{k}}\vec{v}_{\vec{k}} \left(-\frac{\partial f_0}{\partial E}\right) dk \tag{31}$$

$$\sigma_\parallel = \frac{\sigma_0}{1 + \mu^2 B^2}, \tag{32}$$

$$\sigma_\perp = \frac{\sigma_0 \mu B}{1 + \mu^2 B^2}, \tag{33}$$

$$\alpha_0 = e \int \tau(\vec{k})\vec{v}_{\vec{k}}\vec{v}_{\vec{k}} \left(-\frac{\partial f_0}{\partial T}\right) dk, \tag{34}$$

$$\alpha_\parallel = \frac{\alpha_0}{1 + \mu^2 B^2}, \tag{35}$$

$$\alpha_\perp = \frac{\alpha_0 \mu B}{1 + \mu^2 B^2}, \tag{36}$$

using the mobility μ which is proportional to the scattering time τ and inversely proportional to the effective charge carrier mass.

3 Measurement setup

For direct measurements of the Seebeck- and Nernst effect by voltage measurements, a model setup is introduced based on the phenomenological equations that were derived in the previous chapter:

$$U_y = (S_A - S_B)\Delta T_y, \tag{37}$$

$$U_x = N H_z \Delta T_y \frac{\Delta x}{\Delta y}. \tag{38}$$

Additionally, mathematical models and optimization are given to correctly calculate the Seebeck and Nernst coefficients based on dynamic voltage measurements. Then the practical realization of the model setup is presented, followed by the sample synthesis, preparation and installation.

3.1 Model setup

The model setup displayed in Figure 4 consists of the following components: a sample of material X, two R-type thermocouples, three copper wires and two dual channel nanovoltmeters that can measure four different voltage signals in total. The heads of two R-type thermocouples touch the sample along the y-direction from the bottom, while the copper wires are attached at the top of the sample. Additionally, an external magnetic field can be applied in the z-direction, while a temperature gradient can be created along the y-direction of the sample. In total there are five different contact points of wires with the sample, each having an individual temperature. It is assumed that small temperature gradients in the x-direction, that can occur in a real experiment, are negligible compared to the temperature gradient in y-direction resulting in $T_3 \approx T_4$ and $T_5 - T_4 >> T_4 - T_3$. Using Equations 37 and 38 one can explicitly write down the voltages measured by each channel of the sketched voltmeters for a given temperature gradient and magnetic field:

$$U_{\mathrm{Ch1A}} = (S_X - S_{\mathrm{Cu}})(T_5 - T_4) + N H_z \frac{\Delta x}{\Delta y}(T_5 - T_4), \tag{39}$$

$$U_{\mathrm{Ch2A}} = (S_X - S_{\mathrm{Cu}})(T_5 - T_4), \tag{40}$$

$$U_{\mathrm{Ch1B}} = (S_X - S_{\mathrm{Pt}})(T_2 - T_1), \tag{41}$$

$$U_{\mathrm{Ch2B}} = (S_X - S_{\mathrm{Rh13Pt}})(T_2 - T_1). \tag{42}$$
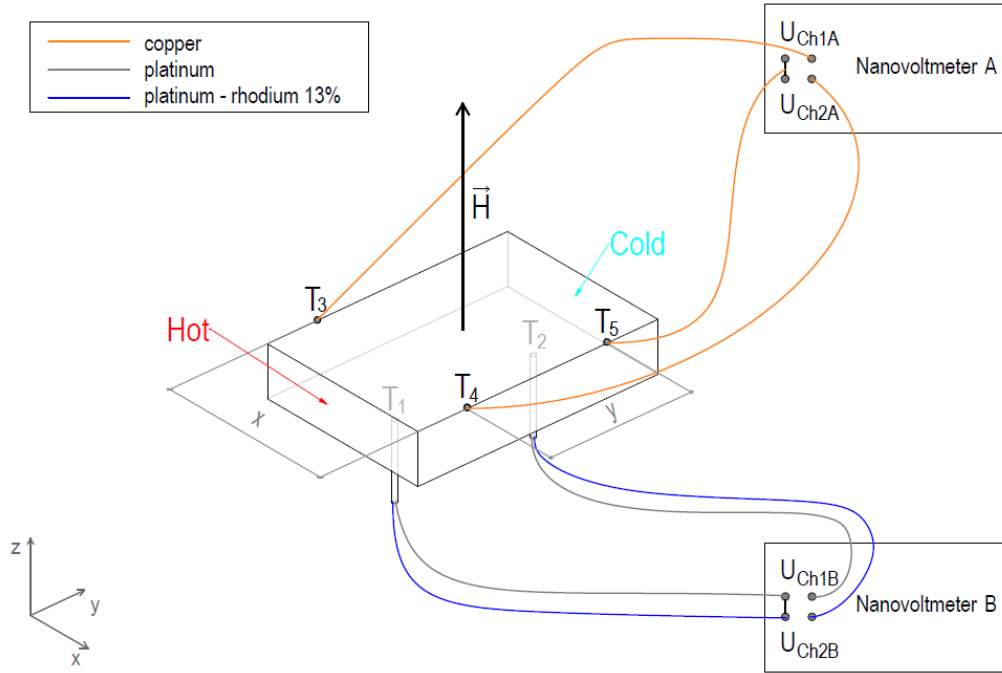
Figure 4: Model setup for simultaneous Nernst- and Seebeck measurements. The sample is connected to two nanovoltmeters via with two R-type thermocouples attached to the bottom, each containing a pair of Platinum and Platinum-Rhodiom 13 wire, and three copper wires attached to the top. The measured voltages have the values $U_{\text{Ch1A}}, U_{\text{Ch2A}}, U_{\text{Ch1B}}, U_{\text{Ch2B}}$. Each wire contact point with the sample has an individual temperature T_1, T_2, T_3, T_4, T_5. The magnetic field is applied in the z-direction, while a temperature gradient is created along the y-direction, indicated by hot and cold.

3.1.1 Calculating the Seebeck coefficient

Combining equation (41) and equation (42) yields an equation for the Seebeck coefficient of the sample X that does not require the knowledge of the individual temperature values T_1 and T_2:

$$S_{\text{X}} = S_{\text{Rh13Pt}} - \frac{S_{\text{Rh13Pt}} - S_{\text{Pt}}}{1 - \frac{U_{\text{Ch1B}}}{U_{\text{Ch2B}}}}. \tag{43}$$

For the chosen R-type thermocouples the factor $S_{\text{Rh13Pt}} - S_{\text{Pt}}$ can be calculated for each temperature by differentation of the NIST reference table [12] with respect to temperature. S_{Pt} is calculated by a fit of experimental data for 70 K $< T <$ 1500 K given by [13]

$$S_{\text{Pt}} = 0.186T[e^{\frac{-T}{88}} - 0.0786 + \frac{0.43}{1 + (\frac{T}{84.3})^4}] - 2.57. \tag{44}$$
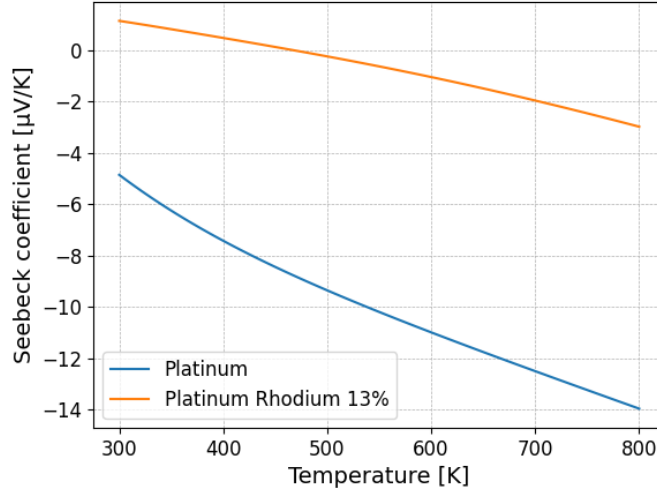
Figure 5: Seebeck coefficients of the R-type thermocouple components as a function of temperature.

3.1.2 Calculating the Nernst coefficient

Similar to the previous calculations dividing equation (26) by equation (27) yields

$$\frac{U_{\text{Ch1A}}}{U_{\text{Ch2A}}} = 1 + \frac{\Delta x}{\Delta y}\left(\frac{NH_z}{S_{\text{Cu}} - S_{\text{X}}}\right). \tag{45}$$

The dependence on individual temperatures can then be eliminated by comparing the equation for two measurements at different values of H_z. By choosing $H_z = 0$ for one of them, which corresponds to a reference measurement without magnetic field, the equation simplifies to

$$\frac{U_{\text{Ch1A}}}{U_{\text{Ch2A}}}(H_z) - \frac{U_{\text{Ch1A}}}{U_{\text{Ch2A}}}(0) = \frac{\Delta x}{\Delta y}\left(\frac{NH_z}{S_{\text{Cu}}(H_z) - S_{\text{X}}(H_z)}\right). \tag{46}$$

Solving for N yields

$$N = \frac{\Delta y}{\Delta x}\left(\frac{S_{\text{Cu}}(H_z) - S_{\text{X}}(H_z)}{H_z}\right)\left(\frac{U_{\text{Ch1A}}}{U_{\text{Ch2A}}}(H_z) - \frac{U_{\text{Ch1A}}}{U_{\text{Ch2A}}}(0)\right). \tag{47}$$

$S_{\text{X}}(H_z)$ is calculated by using equation (37) in presence of a magnetic field H_z while $S_{\text{Cu}}(H_z)$ is calculated by using a fit of experimental data for $70\text{ K} < \text{T} < 1500\text{ K}$ given by Ref.[13], also assuming that its dependence on magnetic field is negligible, $S_{\text{Cu}} \approx S_{\text{Cu}}(H_z)$.

$$S_{\text{Cu}} = 0.041T[e^{\frac{-T}{93}} + 0.123 - \frac{0.442}{1 + (\frac{T}{172.4})^3}] + 0.804 \tag{48}$$

3.1.3 Elimination of spurious offset voltages

The measurement equations (30) and (34) tend to give inaccurate results for individual measurement points because of spurious offset voltages that can affect each measured signal differently and independently. These spurious voltages can stem from temperature differences at any electrical connection between different materials or inhomogeneities in the thermocouples and can usually not be completely avoided [14]. Consequently, equations (30) and (34) in their basic form should only be used to obtain a rough estimate for the thermoelectric coefficients S_X and N. The impact of spurious offset voltages becomes obvious if, for example, a small offset voltage δU is added to U_{Ch1B} or U_{Ch2B} in equation (43) yielding

$$S_{\mathrm{X}} = S_{\mathrm{Rh13Pt}} - \frac{S_{\mathrm{Rh13Pt}} - S_{\mathrm{Pt}}}{1 - \frac{U_{\mathrm{Ch1B}}+\delta U}{U_{\mathrm{Ch2B}}}}. \tag{49}$$

For a Seebeck coefficient S_{X} of 100 µV/K at 300 K, the ratio $\frac{U_{\mathrm{Ch1B}}+\delta U}{U_{\mathrm{Ch2B}}}$ can be calculated without offset voltages ($\delta U = 0$).

$$\frac{U_{\mathrm{Ch1B}}}{U_{\mathrm{Ch2B}}} = 1 - \frac{S_{\mathrm{Rh13Pt}} - S_{\mathrm{Pt}}}{S_{\mathrm{Rh13Pt}} - S_{\mathrm{X}}}(T = 300\mathrm{K}) = 1.0606... \tag{50}$$

Even if assumed that offset voltage δU is small compared to the signal U_{Ch2B}

$$\frac{\delta U}{U_{\mathrm{Ch2B}}} = 0.01, \tag{51}$$

the value of S_X changes significantly, if the term that includes δU is considered and used the calculated ratio of $\frac{U_{\mathrm{Ch1B}}}{U_{\mathrm{Ch2B}}}$:

$$S_{\mathrm{X}} = S_{\mathrm{Rh13Pt}} - \frac{S_{\mathrm{Rh13Pt}} - S_{\mathrm{Pt}}}{1 - \frac{U_{\mathrm{Ch1B}}}{U_{\mathrm{Ch2B}}} - \frac{\delta U}{U_{\mathrm{Ch2B}}}} = 86.0143... \ [\mu\mathrm{V/K}]. \tag{52}$$

Looking at the equations it is obvious that the error induced by δU gets more significant the higher the difference of the Seebeck coefficient of the sample compared to S_{Rh13Pt} and S_{Pt} is.

To eliminate the effect of spurious offset voltages it is necessary to take a look at the ratio of U_{Ch1B} and U_{Ch2B} during the relaxation of a temperature gradient across the sample for a measurement done by the realized measurement setup introduced in the next section. The results shown in Figure 7 show excellent linear correlation between U_{Ch1B} and U_{Ch2B}. This allows for the well-known approach to calculate the Seebeck coefficient from a linear fit of U_{Ch1B} and U_{Ch2B} rather than single data points [14] yielding
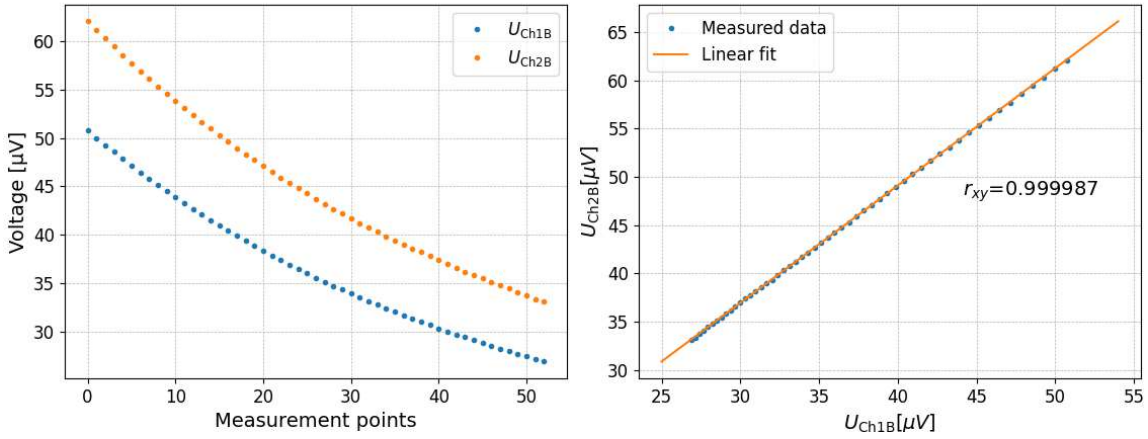
Figure 6: Linear correlation of voltage measurements. U_{Ch1B} and U_{Ch2B} are the voltages values measured by the real experiment equivalent of nanovoltmeter B sketched in Figure 4. r_{xy} represents the Pearson correlation coefficient of the measured signals.

$$S_{\mathrm{X}} = S_{\mathrm{Rh13Pt}} - \frac{S_{\mathrm{Rh13Pt}} - S_{\mathrm{Pt}}}{1 - \frac{\partial U_{\mathrm{Ch1B}}}{\partial U_{\mathrm{Ch2B}}}}. \tag{53}$$

This transition mathematically eradicates errors caused by offset voltages of any source, if they remain constant during each measurement respectively.

The same approach can be made for the calculation of the Nernst coefficient, looking at the ratio between U_{Ch1A} and U_{Ch2A} in equation (15). The linear correlation that was observed for U_{Ch1A} and U_{Ch2A} during the measurements showed equally excellent correlation values as displayed in Figure 6, allowing equation (47) to be rewritten as

$$N = \frac{\Delta y}{\Delta x}\left(\frac{S_{\mathrm{Cu}}(H_z) - S_{\mathrm{X}}(H_z)}{H_z}\right)\left(\frac{\partial U_{\mathrm{Ch1A}}}{\partial U_{\mathrm{Ch2A}}}(H_z) - \frac{\partial U_{\mathrm{Ch1A}}}{\partial U_{\mathrm{Ch2A}}}(0)\right), \tag{54}$$

in order to eradicate constant spurious offset voltages during measurements.

3.1.4 Compensation for transversal temperature gradients and asymmetric contact points

Creating the model setup, it was assumed that small transversal temperature gradients (x-direction) that can occur in a real experiment is negligible compared to the longitudinal temperature gradient (y-direction) that is created on purpose. However, in certain materials suchs as bismuth, with a high Nernst coefficient and strong magnetic-field dependence of the Seebeck coefficient, even small transversal temperature gradients can cause a significant signal contribution. Similar unwanted signal

contributions can occur due to asymmetric contact points at the top of the sample
that can never be completely avoided in the experimental realization of the model
setup.

Assuming a transversal temperature gradient ΔT_{trans} across the sample, an un-
wanted longitudinal Nernst signal would be superimposed onto the voltages that
are measured by the R-type thermocouple attached to the bottom of the sample.
Equations 41 and 42 therefore need to be modified to account for this signal contri-
bution. Rewriting the longitudinal temperature gradient as $\Delta T_{\text{long}} = (T_2 - T_1)$ the
compensated equations can be written as

$$U_{\text{Ch1B}} = (S_{\text{X}} - S_{\text{Pt}})\Delta T_{\text{long}} + N H_z \frac{\Delta y}{\Delta x}\Delta T_{\text{trans}}, \tag{55}$$

$$U_{\text{Ch2B}} = (S_{\text{X}} - S_{\text{Rh13Pt}})\Delta T_{\text{long}} + N H_z \frac{\Delta y}{\Delta x}\Delta T_{\text{trans}}. \tag{56}$$

Assuming the Seebeck-coefficient of a given sample X at a magnetic field of 1 Tesla
is 80 µV/K while the Nernst signal is 20 µV/K equations (55) and (56) can be used
to calculate the respective voltages. The longitudinal and transversal temperature
gradient are assumed to relax exponentially from 2 K and 0.5 K respectively over
the course of 30 data points of U_{Ch1B} and U_{Ch2B}. For simplicity $\frac{\Delta y}{\Delta x} = 1$ will further
be assumed. Figure 7 shows the temperature gradients as well as the calculated
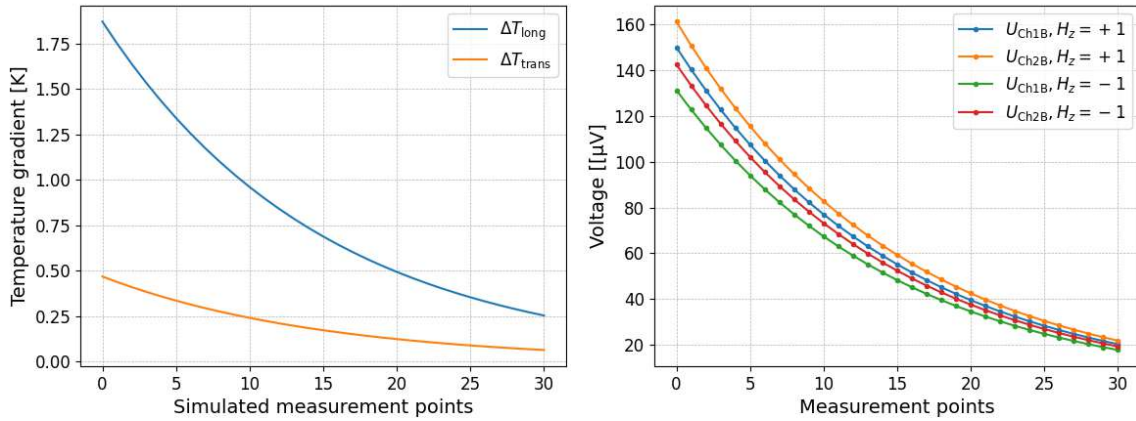voltages.

Figure 7: (Left) Simulated longitudinal and transversal temperature gradients in comparison.
(Right) Simulation of the resulting voltages and their dependence on the magnetic field H_z.

The linear correlation between U_{Ch1B} and U_{Ch2B} is still intact as the additional volt-
age contribution affects both voltages equally. Using equation (53) for calculating

the Seebeck coefficient, two different solutions, depending on the direction of the magnetic field, occur, because the original formula does not take the superimposed signals into account:

$$S_{\mathrm{X}}(H_z = +1) = 85\ \mathrm{\mu V/K}, \tag{57}$$

$$S_{\mathrm{X}}(H_z = -1) = 75\ \mathrm{\mu V/K}. \tag{58}$$

It immediately becomes clear that the correct value of the Seebeck coefficient can be obtained by taking the mean value of the calculated values above, effectively cancelling the unwanted signal contribution.

Similar symmetry considerations can be made for potential misalignments of the wire contacts at the top of the samples yielding additional signal contributions in U_{Ch1A} and U_{Ch2A}. Consequently, equation (54) can still be used to correctly calculate the Nernst coefficient by taking the mean value of the calculated values for both directions of the magnetic field.

It is important to note that this symmetry property can only be exploited for samples that do not show any anisotropy in the Seebeck- and/or Nernst coefficient and only for consistent, reproducible temperature gradients.

3.2 Realization of the model setup

This section introduces the actual measurement setup at TU Wien, which aims at realizing the model setup introduced in the previous chapter. Additionally, basic information about all the required measurement devices is provided.

3.2.1 Magnet and vacuum setup

To produce magnet fields up to 12 T a Nb-Ti coil is used that reaches its superconducting state at around 9.5 K. To reach this temperature a Glifford-Mc-Mahon refrigerator is used, while liquid helium is transported by a Sumitomo F-50 compressor. The coil has a cylindrical space with an inner diameter of 65 mm that is externally accessible. This space is filled with a metal tube system that can be evacuated up to 10^{-6} mbar by a Pfeiffer HiCube vacuum pump. To prevent the high temperatures of the sampleholder impacting the low temperature of the magnet, the metal tube is additionally cooled by water and air from the outside.

Figure 8: Magnet and vacuum pump setup with inserted sample holder. The cylindrical space inside the coil is filled with an externally water- and air cooled tube system that can be evacuated up to 10^{-6} mbar.

3.2.2   Sample holder

The sample holder was designed with the following goals in mind:

- **Implementing the model setup**: As the mathematical models introduced in 3.1 are based on the model setup, the sample holder needs to recreate it as close as possible.

- **Consistent and valid measurement results**: Measurement results should be consistent, contain low noise and replicate published reference values of the Seebeck- and Nernst coefficient.

- **High temperature and high field application**: Measurements at temperatures up to 600 K and magnetic fields up to 10 Tesla should be possible without any safety issues or causing damage to the sample holder.

- **Ease of use**: Changing the sample and maintaining the sample holder should be easy and require little to no training.

- **Variation of sample dimensions**: The sample holder should allow different width, length and thickness of samples in a reasonable range.

To achieve these goals the sample holder was constructed as follows. It consists of two copper blocks that are mounted to a long brass bar. The top copper block contains two large vertical cylindrical holes to mount two heating cartridges to control the base temperature of the sample. Additionally, two central vertical small cylindrical holes guide the thermocouples through the copper block to provide contact with the sample. On one side a small cylindrical hole mounts a PT-100 resistance sensor to measure the base temperature of the copper block. At the top of the block a thin MACOR plate [15] is used to assure proper thermal connection of the sample to the copper block, but secure electrical isolation from each other. At the top of the MACOR plate and underneath one end of the sample, a DMS is affixed using high temperature cement that is used to create a temperature gradient along the sample. The plate also consists of two small holes following the channels in the copper block to connect the sample with both thermocouples from underneath which measure U_{Ch1B} and U_{Ch2B}. U_{Ch1A} and U_{Ch2A} are measured by three wires that are directly connected to the sample by spot welding prior to each measurement. To fixate the sample from the top, up to two additional MACOR plates can be used. Further down the second copper block contains springs that ensure proper contact pressure of the thermocouples and the sample. Variation of its position by moving the corresponding nuts can be used to increase or decrease the contact pressure. The possible sample dimensions of the sample holder are summarized in table 1.

Figure 9: Overview of the sample holder.
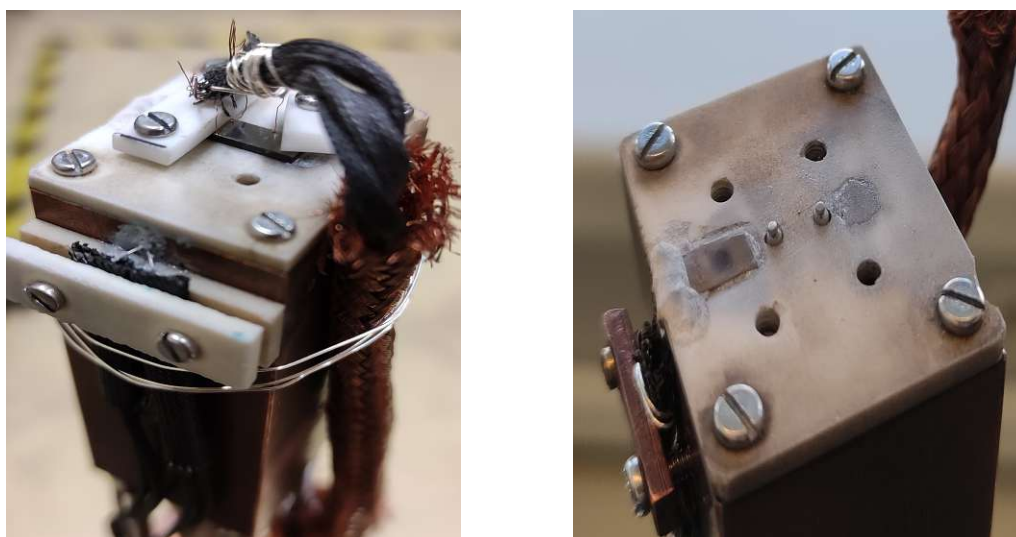
Figure 10: Head of the sample holder with (left) and without (right) an installed sample.

Sample dimensions			
Dimension	Min [mm]	Max [mm]	Recommended [mm]
Length	10	20	15
Width	1	5	4
Height	0.5	2.5	1

Table 1: Sample dimensions supported by the sample holder.

3.2.3 Nanovoltmeters

For all measurements of $U_{Ch1A}, U_{Ch2A}, U_{Ch1B}$ and U_{Ch2B} Keithley 2182A nanovolt-meters are used. The 2182A model is optimized for making stable, low noise voltage measurements and for characterizing low resistance materials and devices reliably and repeatably[16].
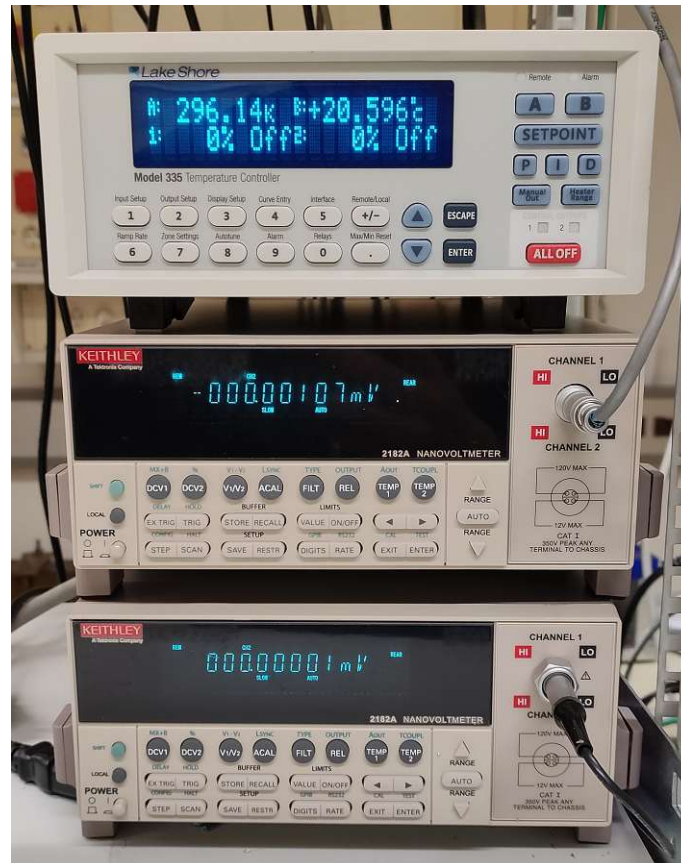
Figure 11: Keithley 2182A and LS335 Temperature Controller.

3.2.4 Temperature Controller

The Lakeshore 355 Temperatur Controller provides two individual heater outputs as well as two individual sensor input connectors. Each sensor can be assigned to each output to create and hold a specific target temperature for example. For this setup Sensor A is assigned to Out 1 to control and monitor the base temperature of the copperblock and the thermally connected sample. Out 2 is used to control the current flow through the DMS to create a temperature gradient along the sample. Sensor B is monitoring the temperature outside of the metal tube system.

Figure 12: LS335 Temperature Controller Rear Pannel [17]

3.2.5 Connection details of the sample holder

Apart from the thermocouple wires, copper wires were used to connect the sample holder with two 16 pole output Fischer connectors, mounted on a plate. All wires were thermally and electrically isolated by fibreglass tubes and screened by pure copper screens. Additionally, each wire pair was twisted against each other to reduce cross-talk and external electromagnetic interference. Figure 13 shows the connections on the outside of the sample holder. The red dots indicate the orientation. The connections with the nanovoltmeters are done as modeled in section 3.1.
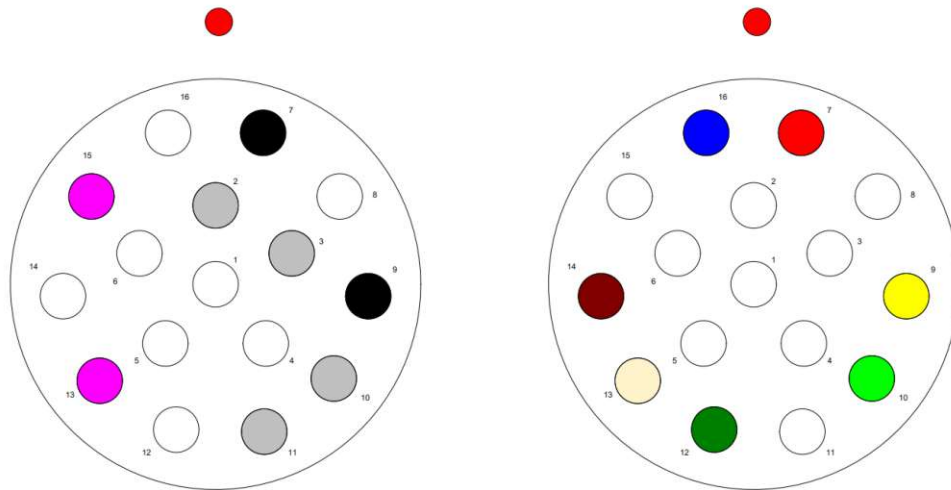

Figure 13: Contacts of the Fischer connector from the outside. The red dots outside of the connector are indicators for the orientation of the installation of the sample holder.

Position 13 and 15 (magenta) connect the parallel wired heating cartridges with to Output 1 of the Temperature Controller. Position 7 and 9 (black) connects the DMS

to Output 2 of the Temperature Controller. The wires of the Pt-100 temperature sensor (grey) lead to 6-pin DIN connector that is connected with Input A of the Temperature Controller. Position 14 (dark red) is connected to both channels of nanovoltmeter A while position 13 (creme) and position 14 (dark green) are connected to channel 1 and channel 2 of nanovoltmeter A respectively. Position 16 and 10 (blue and green) connect the platinum wires of each of the thermocouples to channel 1 of nanovoltmeter B while position 7 and 9 (red and yellow) connect the platinum-rhodium wires to channel 2.

3.2.6 Sample installation

To properly install a sample of dimensions within the given boundaries on the sample holder, the following steps need to be followed for each measurement.

- **Cleaning the DMS and thermocouple heads**: Before starting a new measurement all remains of thermal grease from a previous measurement must be removed with a cotton swab and minimal amount of ethanol. To ensure excellent connection between the sample and the two heads of the thermocouples, they are cleaned with cotton swabs and slightly polished with fine sandpaper.

- **Polish and clean the sample**: Both sides of the sample need to be polished with fine sandpaper and afterwards should be cleaned with ethanol.

- **Applying thermal grease**: To ensure proper thermal connection of the surface of the DMS heater and the sample, a small amount of thermal grease is evenly applied on the DMS. For all measurements performed as part of this diploma thesis, silicon thermal grease products with a thermal conductivity between 3.9 and $5.2 \frac{W}{mK}$ were used.

- **Connecting the copper wires to the sample**: The three copper wires of the sample holder are spot welded on top of the sample. This process is always done with the assistance of a light microscope to target symmetrical contacting as shown in the model in Figure 4.

- **Placing and securing the sample**: The sample is placed on top of the sample holder as shown in Figure 14 and afterwards fixed using the intended screws and MACOR piece. The screws should be gently tightened until slight resistance occurred. Depending of the length of the sample and the placement of welding spots of the copper wire contacts, a half or full sized second MACOR piece can be used.
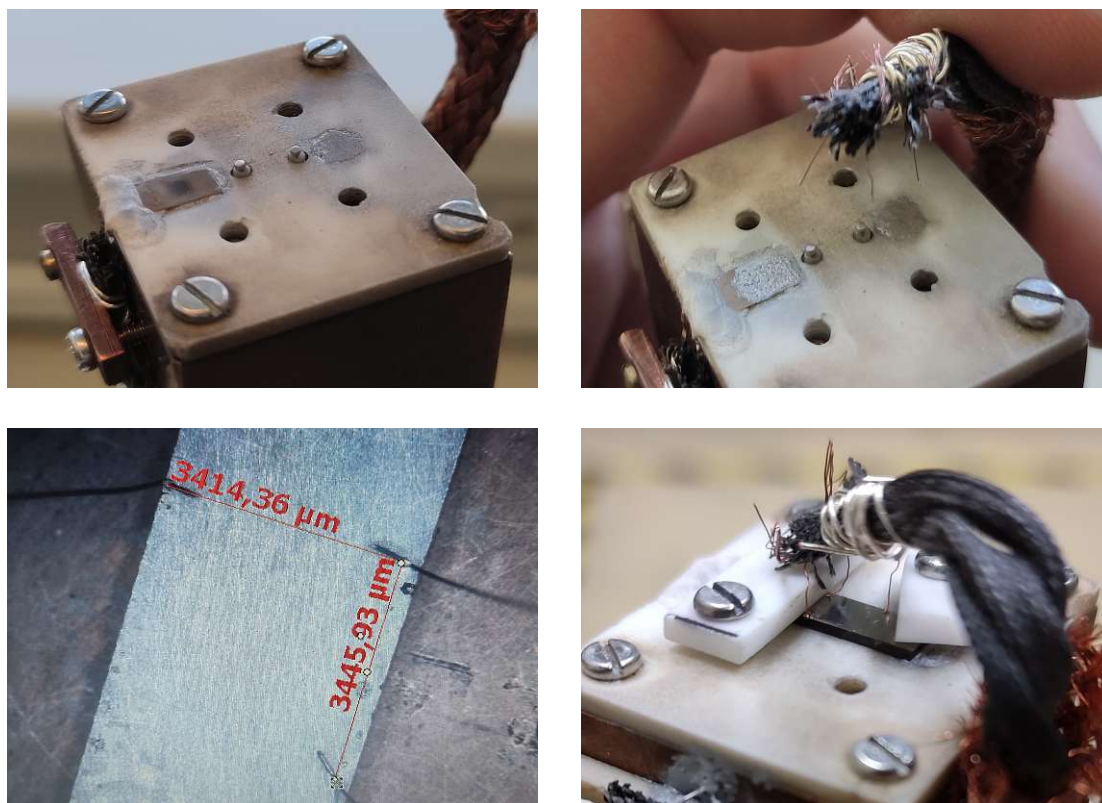
Figure 14: Steps of the sample installation. Sample holder after cleaning with ethanol and cotton swab (top left). Applied thermal grease and prepared wires (top right). Spot welding contacts (bottom left). Installed sample (bottom right).

3.2.7 Installation of the sample holder

Once the sample is properly installed, the sample holder can be inserted into the cylindrical tube system inside the coil of the magnet. After fixing the sample holder, the Fischer connectors are connected and the vacuum pump is started to evacuate the tube until a stable vacuum of about 10^{-6} mbar is reached.

Figure 15: Installation of the sample holder. Tube system ready for insertion of the sample holder (left). Installed and fixed sample holder (middle). Connected wires (right).

4 Measurement process and automation

This chapter introduces the measurement process and its automation by design and implementation of a designated measurement software.

4.1 Steps of the measurement process

Having identified the correct measurement equations for the Seebeck- and Nernst Effect:

$$S_{\mathrm{X}} = S_{\mathrm{Rh13Pt}} - \frac{S_{\mathrm{Rh13Pt}} - S_{\mathrm{Pt}}}{1 - \frac{\partial U_{\mathrm{Ch1B}}}{\partial U_{\mathrm{Ch2B}}}} \tag{59}$$

$$N = \frac{\Delta y}{\Delta x} \left(\frac{S_{\mathrm{Cu}}(H_z) - S_{\mathrm{X}}(H_z)}{B_z} \right) \left(\frac{\partial U_{\mathrm{Ch1A}}}{\partial U_{\mathrm{Ch2A}}}(H_z) - \frac{\partial U_{\mathrm{Ch1A}}}{\partial U_{\mathrm{Ch2A}}}(H_z = 0) \right) \tag{60}$$

it is needed to create the measurement conditions discussed in previous chapters and measure the voltage signals $U_{\mathrm{Ch1A}}, U_{\mathrm{Ch2A}}, U_{\mathrm{Ch1B}}, U_{\mathrm{Ch2B}}$ to determine the Seebeck- and Nernst Coefficient of a given sample. Each measurement cycle is separated into several steps for clarification. Figure 16 shows a flowchart of the process, while Figure 17 shows the progress of the base temperature of the copper block attached to the sample holder, temperature gradient of the sample and magnetic field for one measurement cycle.
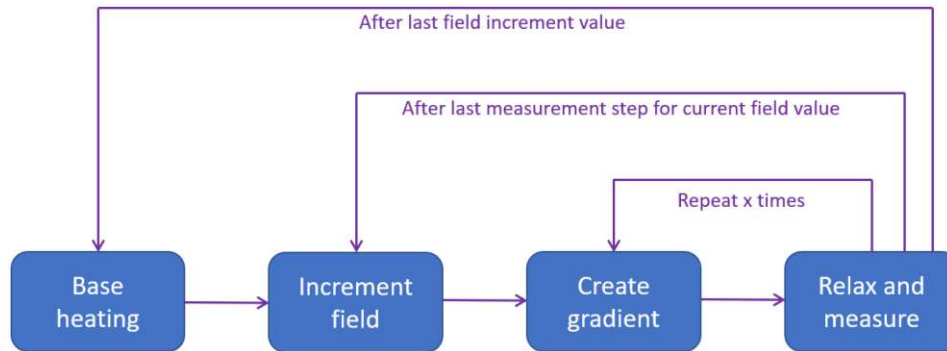

Figure 16: Flowchart of the measurement process.

- **Step 1: Base heating**
  Target base temperature of the copper block of the sample holder and the thermally connected sample is set and stabilized by the temperature controller via the cartridge heaters and using the PT-100 as a sensor of the sample holder.

- **Step 2: Increment magnetic field**
  The magnetic field is set to its next designated value.

- **Step 3: Create a temperature gradient**
  After the measurement system has reached a stable base temperature and the incrementation of the magnetic field is finished, a temperature gradient along the sample is created by applying a constant current flow through the DMS. Once the desired temperature gradient (typically 1-3 K) is reached, the voltage measurements can begin.

- **Step 4: Measure voltages while relaxing the temperature gradient**
  The constant current flow through the DMS is stopped and the voltages are measured simultaneously while the gradient is being relaxed. Depending on the number of voltage measurement points, this process usually takes about 20 to 60 seconds. After repeating this procedure for a desired number of times, the process continues with Step 2 or Step 1 if the last field incrementation value was reached.
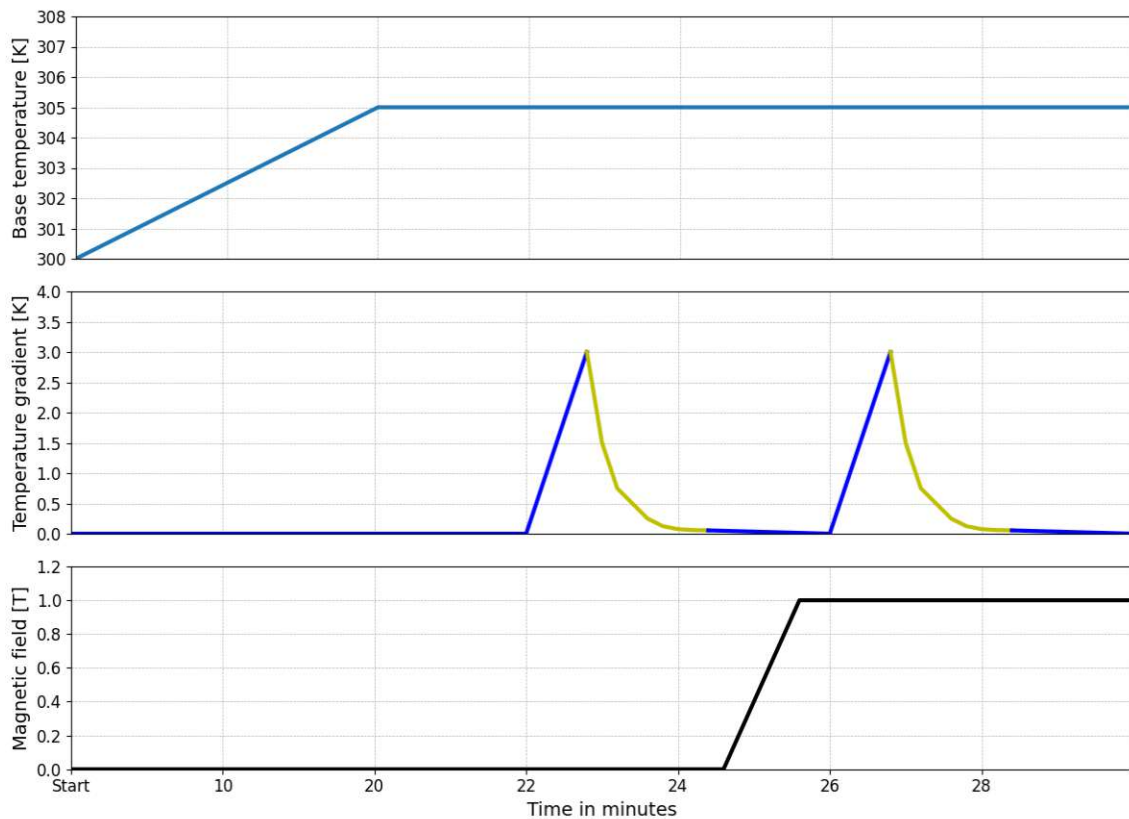

Figure 17: Illustration of the measurement process with typical parameters.

4.1.1 Quasi-simultaneous voltage measurements

To correctly calculated the derivatives in the measurement equations (17) and (18) it is required to measure U_{Ch1A} and U_{Ch2A} as well was U_{Ch1B} and U_{Ch2B} simultaneously. Due to the lack of a second ADC inside the unit the Keithley 2182A nanovoltmeter can only measure the signals of its channels consecutively. Consequently, data interpolation is required. Because the time between the measurement of the separate channels is small and constant, a simple model of data interpolation, often referred to as delta method, can be used. This method becomes exact as the time difference between the measurements between both channels of the nanovoltmeter approaches zero. As shown in Figure 18 the final values used for further calculations can be
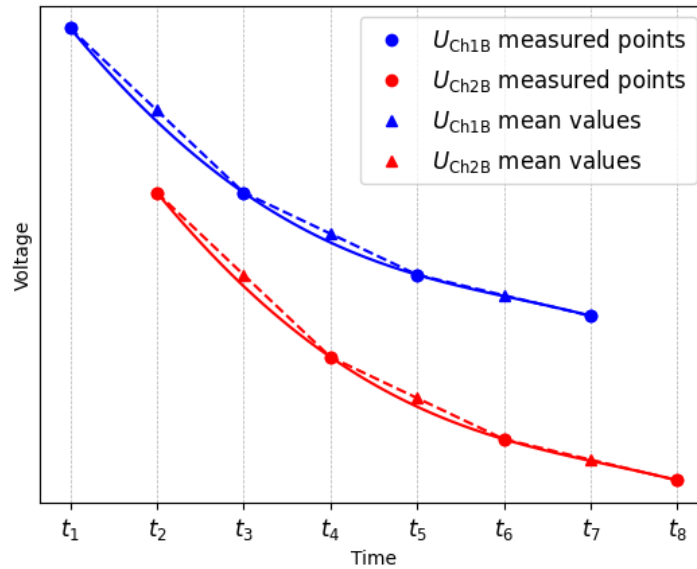

Figure 18: Delta method for quasi-simultaneous voltage measurements.

written as follows:

$$U_{\mathrm{Ch1B}} = [\frac{U_{\mathrm{Ch1B}}(t_1) + U_{\mathrm{Ch1B}}(t_3)}{2}, U_{\mathrm{Ch1B}}(t_3), \frac{U_{\mathrm{Ch1B}}(t_3) + U_{\mathrm{Ch1B}}(t_5)}{2}, U_{\mathrm{Ch1B}}(t_5), ...]$$

$$U_{\mathrm{Ch2B}} = [U_{\mathrm{Ch2B}}(t_2), \frac{U_{\mathrm{Ch2B}}(t_2) + U_{\mathrm{Ch2B}}(t_4)}{2}, U_{\mathrm{Ch2B}}(t_4), \frac{U_{\mathrm{Ch2B}}(t_4) + U_{\mathrm{Ch2B}}(t_6)}{2}, ...]$$

In general, the information of $U_{\mathrm{Ch1B}}(t_1)$ and $U_{\mathrm{Ch2B}}(t_N)$ is obviously lost during this method, which can be neglected when using a lot of data points. Since the values of U_{Ch1B} and U_{Ch2B} are now synchronized in time, they can be used to properly calculate the derivatives in equation (17). For the calculating the derivatives in the formula of the Nernst coefficient the same model is applied to U_{Ch1A} and U_{Ch2A} for synchronization of the signals.

4.2 Software and graphical user interface

To fully automate the measurement steps introduced in the previous chapter, a user friendly measurement software and graphical user interface was programmed and designed using Python. To keep the measurement setup expandable, the software is split into layers with well defined communication channels.

4.2.1 Connection of measurement devices

Both nanovoltmeters as well as the temperature controller are connected by a Serial-to-USB Interface to a PC running a Lubuntu Linux distribution. The base communication of the devices is made possible by individually programmed drivers. These contain device specific commands that control defined actions of the measurement devices. Sending a command triggers a reaction of the measurement device that can lead to an answer.

4.2.2 Measurement devices as socket servers

The devices mentioned above were implemented as socket-servers. For convenience they are from now on only referred to as sockets. For practical use, the sockets were additionally embedded as Linux services in the operating system. The sockets combine several methods defined by each measurement device driver in functions and create a bidirectional communication channel. Return values of the measurement devices are formatted for further usage. For comfortable use of the sockets, an already existing service manager with graphical user interface was extended with entries for the services corresponding to the respective sockets. The service manager can be used to start and stop individual services as well as test their functionality.

Figure 19: sm-tree Servicemanager. Each service offers various requests to test its functionality and can be started and stopped individually.

The sockets the measurement system uses are:

- **magnet** - Control of the magnetic field.

- **TempCtrl** - Control of the base temperature and temperature gradient.

- **Nernst** - Readings and data analysis of the nanovoltmeter that measures U_{Ch1A} and U_{Ch2A} .

- **Seebeck** - Readings and data analysis of the nanovoltmeter that measures U_{Ch1B} and U_{Ch2B}.

4.2.3 Measurement program

The measurement program was designed to model and automate the measurement process introduced in chapter 4. In general, the measurement program is split into two classes. Its basis is implemented as a socket as well. To start the measurement program two configurations files are required. The first one contains basic information of the main socket, for example, a list of sockets that are going to be communicated with. The second configuration file contains all parameters of the sample and the measurement process itself. The second class of the program is responsible for the measurement itself and starts the measurement thread after initialization of all the required sockets. Inside this measurement thread, the program jumps between several measurement states, which correspond to the process steps introduced in chapter 4.

4.2.4 Program start and graphical user interface

The measurement program can be launched by clicking its designated icon located on the desktop.
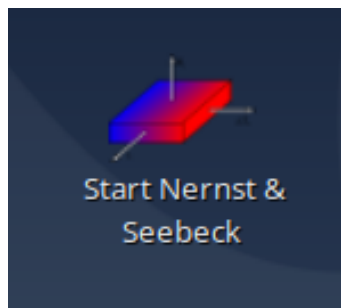

Figure 20: Start icon used to launch the measurement program.

Before launching the graphical user interface, two helpful tools as well as the service manger are started to check the current state of the setup. The first tool displays the temperature of the magnet at various stages. Before starting a measurement it is important to check whether all values except for Stage 1 are well below the critical temperature of the coil (9.5 K). Figure 21 shows the usual temperature values if the magnet is functioning properly. The second one displays the current base temperature of the copper block as well as the temperature of the outside of the tube. It also displays active heating processes as well as the output power of the respective heaters. Additionally, the current magnetic field and state of the magnet are displayed.
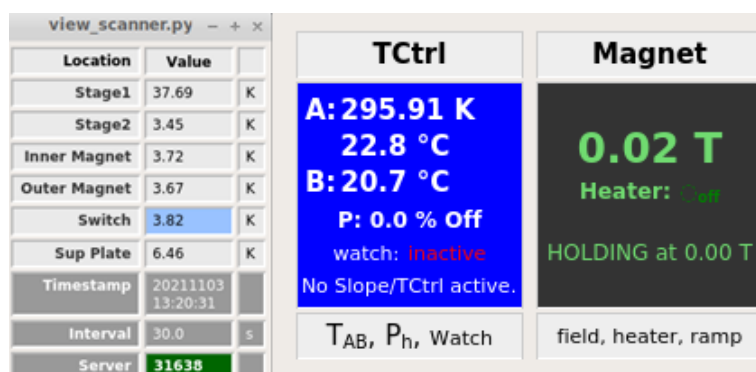
Figure 21: Additional monitoring tools used to check for the current state of the measurement setup.

The graphical user interface is designed to fill the second configuration file mentioned in the previous section as well as configure the output file of the measurement. The various options will now be discussed in detail. Simplified versions of the descriptions below can be displayed by hovering the cursor over the respective field names.
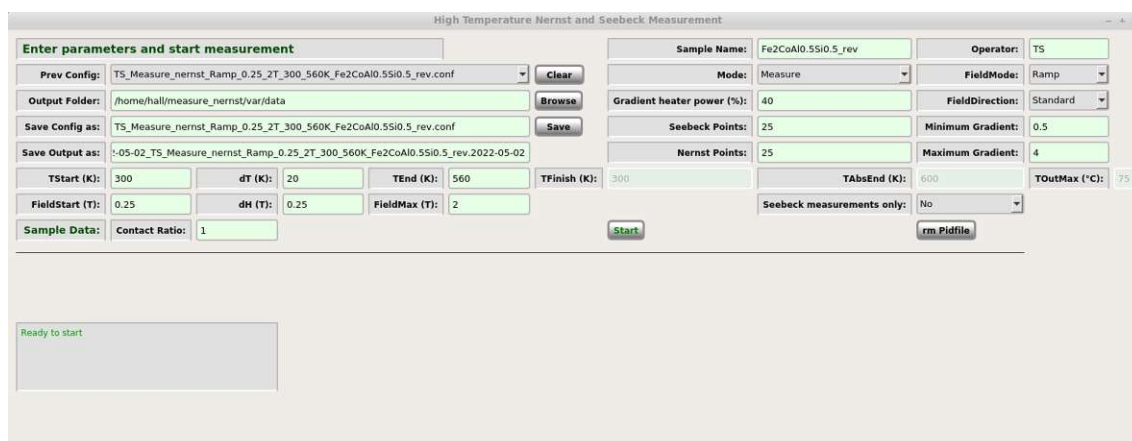

Figure 22: Graphical User Interface.

- **Prev Config**: Displays a drop-down list of previous measurement configurations that can be loaded. The *Clear* button deletes all previous configurations.

- **Output Folder**: Direction where the Output file will be stored. A default path is given that can be changed by the Browse button

- **Save Config as**: Lists the name of the configuration file. It is automatically created and updated dependent on various measurement parameters to easily distinguish different measurements of the same sample.

- **Save Output as**: Similar to the configuration file, the name of the output file is created and updated dependent on various measurement parameters.

- **Sample name**: Used to enter the name of the sample. Updates the name of the configuration- and output file.

- **Operator name**: Used to enter the operator name. Updates the name of the configuration- and output file.

- **Mode**: Can be set to *Measure* to start a real measurement or *Simulate* to test the functionality of the program without starting the base or gradient heater or applying a magnetic field.

- **Field Mode**: Controls the way the magnetic field is set. Can be set to *Ramp* or *Constant*. *Constant* should only be used if you only want to measure the Seebeck coefficient at a constant magnetic field or without any magnetic field at all.

- **Field Direction**: Can be set to *Normal* or *Reverse*. This setting must always correspond with the red switch at the backplane of the magnet power supply for correct measurement values.

- **Gradient heater power**: Controls the power of the gradient heater. Values between 20 and 40 are recommended.

- **Seebeck Points / Nernst Points**: Sets the amount of measurement points taken during the relaxation of the gradient. Values between 20 and 40 are recommended.

- **Seebeck measurments only**: Can be set to *Yes* to force the measurement system to only take Seebeck coefficient measurements.

- **Minimum Gradient / Maximum Gradient**: Forces the gradient heater to target a specific temperature gradient in the given range before it is relaxed.

- **TStart**: Sets the base temperature for the first measurement cycle.

- **TEnd**: Sets the base temperature for the last measurement cycle.

- **TFinish**: Target base temperature after the measurement is finished or interrupted. This value is usually set to 300 K and only edited for special applications.

- **TAbsEnd**: Once the set maximum value of base temperature of the copper block is reached, the Temperature controller and all heating processes are immediately shut off. This value is experimentally determined and set for safety reasons and should therefore only be edited for special applications.

- **TOutMax**: In case of an outage of the vacuum pump, air may leek into the tube and form a thermal connection between the copper block and the tube. Once the set maximum value of temperature of the outer tube is reached the Temperature controller and all heating processes are immediately shut of. This value is experimentally determined and set for safety reasons therefore should only be edited for special applications.

- **FieldStart**: Sets the first magnetic field point for each measurement cycle.

- **FieldMax**: Sets the last magnetic field point for each measurement cycle.

- **dT**: Sets the temperature step size between TStart and TEnd

- **dH**: Sets the magnetic field step size between FieldStart and FieldMax

4.2.5 Output files and automatic plots

The output file generated by the measurement program is a simple but structured .txt file. The file is updated after each individual measurement. At the start of the file an informational header is automatically created that displays all entered values of the measurement parameters. Afterwards each measurement is represented by a data line with several columns that are now introduced.

- **Counter**: Ascending number indexing each individual measurement.

- **Cycle**: Ascending number indexing each measurement cycle.

- **Time**: Time at which the first measurement point of each individual measurement was taken.

- **H** [T]: Magnetic field in Tesla.

- **Ts** [K]: Base temperature of the sample.

- **dT** [K]: Gradient at the bottom of the sample before relaxation.

- **ddT** [K]: Change of the gradient at the bottom of the sample during the measurement.

- **N1**[μV/KT] / **NH1**[μV/K]: Nernst Coefficient / Nernst signal. Both values are not compensated for a potential dependence of the Seebeck effect on the magnetic field.

- **N2**[μV/KT] / **NH2**[μV/K]: Nernst Coefficient / Nernst signal. Both values are compensated for a potential dependence of the Seebeck effect on the magnetic field.

- **corN**: Pearson correlation coefficient of U_{Ch1A} and U_{Ch2A}.

- **S**[μV/K]: Seebeck coefficient.

- **corS**: Pearson correlation coefficient of U_{Ch1B} and U_{Ch2B}.

Based on these data sets a separate python program is called after each measurement cycle to generate plots and update them after each following cycle. The program can also be used in a stand-alone mode. The plots are stored in the same direction as the output file and are formatted in a similar way to those presented in the following chapter.

5 Samples and measurement results

This chapter presents the synthesis, preparation process and measurement results for all samples.

5.1 Sample preparation

This section outlines the sample preparation process. At first the sample synthesis is discussed before presenting the annealing and cutting process.

5.1.1 Synthesis

Apart from Constantan, all samples measured in this diploma thesis were created by synthesis at the Institude of Solid State Physics (IFP). At first stoichiometric calculations were made followed by weighing all components with a high precision scale. All used elements have a purity of at least 99.9%. Due to the lower boiling point of Mn (2300 K), compared to the other elements in the alloy it is used in and based on experience, an additional 0.075g of Mn was added for $Co_2MnAl_{0.63}Si_{0.37}$, which ads up to about 5% more Mn than the calculated value in table 2.

Figure 23: High precision scale for weighing the of sample components.

The samples were melted using a high-frequency induction melting system at IFP, creating polycrystalline bulk samples. For this process, all sample pieces are placed in a water cooled copper boat inside an evacuated quartz glass tube which is surrounded by the coil. After evacuation the tube is filled with an overpressure of argon gas. The samples are then heated and molten by inducing eddy currents into the sample material via the high voltage, high frequency coil. Each sample was melted about 5 times.

Co$_2$Mn/Fe$_2$CoAl$_x$Si$_{1-x}$ stoichiometry						
Sample	m [g]	Fe [g]	Co [g]	Mn/Ni [g]	Al [g]	Si [g]
Co$_2$MnAl$_{0.63}$Si$_{0.37}$	5	-	2.943795	1.372115	0.424546	0.259542
Fe$_2$CoAl	6	3.592683	1.584892	-	0.822423	-
Fe$_2$CoAl$_{0.5}$Si$_{0.5}$	6	3.582641	1.580462	-	0.410062	0.426832
Fe$_3$Al	6	4.30644	-	-	0.69355	-
Fe$_3$Al$_{0.5}$Si$_{0.5}$	6	4.294265	-	-	0.345796	0.359938

Table 2: Stoichiometric analysis of cobalt- and iron based based alloys.
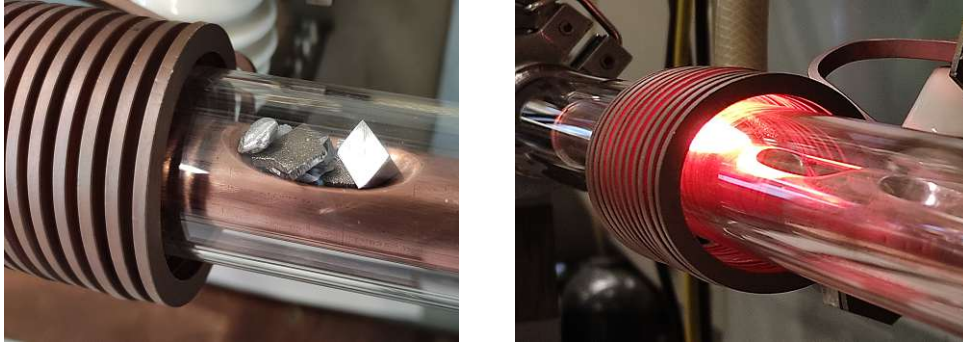
Figure 24: (Left) Sample pieces before melting. (Right) sample during melting.

5.1.2 Annealing

In order to control potential disorder and to homogenize possible strains in the material, annealing is a common practice. For this heat treatment process the sample is heated above its recrystallization temperature, but below its melting point and afterwards slowly cooled or quenched. The effects of annealing on materials varies strongly and is a current topic of research. It should be seen as an experimental technique rather than a strict preparation process, as the parameters such as annealing temperature, cooling progress and overall duration can be individually chosen and experimented with. In this diploma thesis, only Co$_2$MnAl$_{0.63}$Si$_{0.37}$ was annealed before the measurements. To perform the annealing process the sample was vacuum sealed into a quartz glass tube and inserted into an oven. For the other samples synthesized, it was decided to analyse the measurement results at first, before deciding if annealing was necessary to reproduce already published measurement results.

5.1.3   Cutting of the sample

To cut the molten samples into pieces to match the setup dimensions given in Table 1, a Stuers Accutom-100 cutting device [18] was used. The sample was first glued to an arbitrary aluminium block and then inserted into the device. Figure 26 shows the typical cuts that were done to generate multiple samples in chronological order. The sample cones, that were cut of both ends, were used for structural XRD-analysis that will be provided along with the measurement results.

Figure 25: Struers Accutom 100 cutting device.
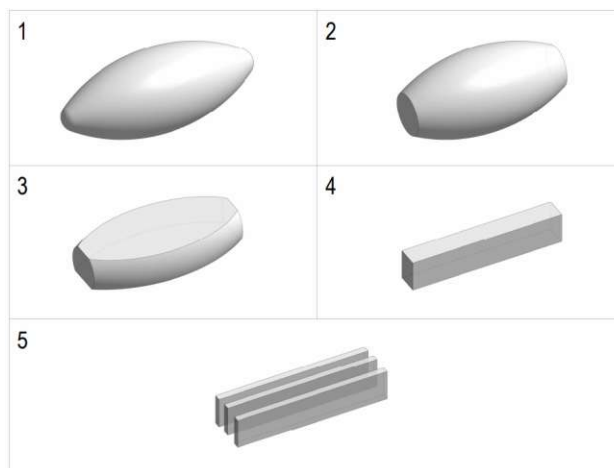
Figure 26: Schematic diagram of the chronological cuts that were made using the Streuer Accutom 100.

5.2 Measurement results

This sections provides the measurement results for the Seebeck- and Nernst measurements performed with the presented measurement setup for each sample. The measurement system was tested for magnetic fields up to 10 Tesla and temperatures up to 560 K. Depending on the melting point of the sample and lack of reference data for high magnetic fields and high temperatures, the chosen temperature and magnetic field ranges were set for each sample individually. For base characterization of the crystal structure and homogeneity, X-ray diffraction measurements were performed, except for bismuth and Constantan. In addition, resistivity- and Seebeck measurements were performed using an ULVAC ZEM 3 [19] measurement apparatus, employing the 4-point probe method for additional characterization and reference. The measurement results for each sample are presented in order of X-ray diffraction (only for the Heusler alloys), Seebeck-, resistivity- and Nernst measurements (all samples, except Constantan). Additionally, basic information about each sample and reasoning why it was chosen for a measurement is provided. For all measurements in magnetic fields the compensation ideas introduced in 3.1.4 were applied to calculate the correct Seebeck- and Nernst coefficients from the measurement data, consequently yielding symmetric results for both directions of magnetic field. At the end of this section, all results will be summarized and compared with each other.

5.2.1 Constantan

To verify the accuracy of Seebeck coefficient measurements of the measurement setup, Constantan was chosen as reference material, because reliable reference data of this material exist. Constantan is a proprietary name by VDM Metals for a metallic alloy consisting of approximately 54% copper, 44% nickel and 1% manganese [20]. The name is an indication of the alloys resistivity which remains practically constant over a broad temperature range, making it useful for technical applications. The Constantan sample measured in this work, was included as a reference sample for the ULVAC ZEM-3 measurement apparatus. In Ref.[21] and Ref.[22] reference functions for the Seebeck coefficient from 0 to 400 K that were generated by statistical analysis of measurement results of Constantan, made by 12 different laboratories spread across the world that have active thermoelectric research programs, are provided:

$$S_{\mathrm{C}}(T) = -1.076 + 0.5294 \log(T+1) - 2.22\sqrt{T} + 1.160 \sin(\frac{2\pi T}{700}) + 3.248 \cos(\frac{2\pi T}{700}), \quad (61)$$

$$S_{\mathrm{C}}(T) = -0.09 + 1.81 \log(T+1) - 2.79\sqrt{T} + 0.93 \sin(\frac{2\pi T}{700}) + 1.39 \cos(\frac{2\pi T}{700}). \quad (62)$$

The Seebeck coefficient of Constantan is negative and decreases approximately linear with temperature as shown in Figure 27. The measurement data are in excellent

agreement with the reference function (57) for temperatures between 300 and 400 K. Above 400 K the measurement data follows the reference function (61) indicating the reference function's viability even beyond its designated temperature range. As expected, the ULVAC ZEM-3 resistivity measurements shown in Figure 28 confirm the resistivity being practically constant.
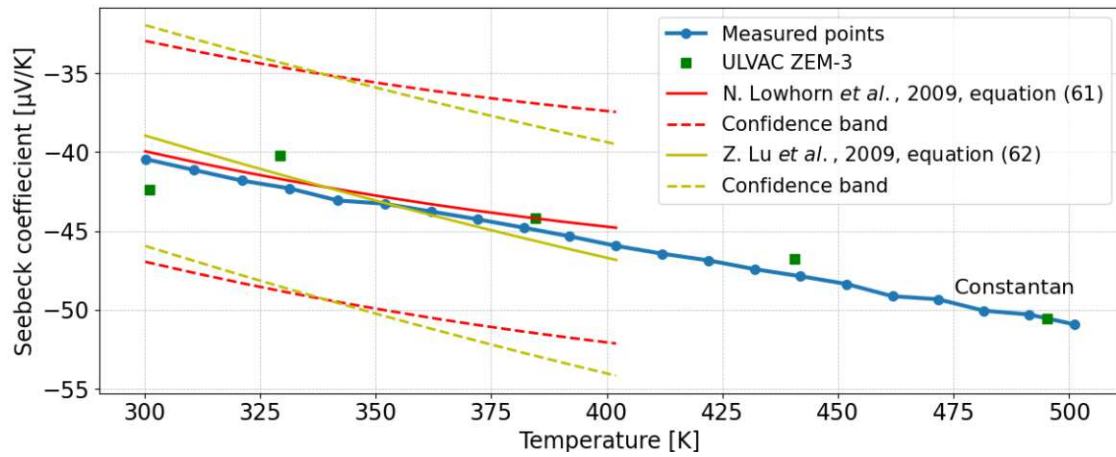

Figure 27: Seebeck coefficient measurement results of Constantan as function of temperature compared with reference data of Z. Lu *et al.* 2009 [21] and N. Lowhorn 2009 *et al.* [22].
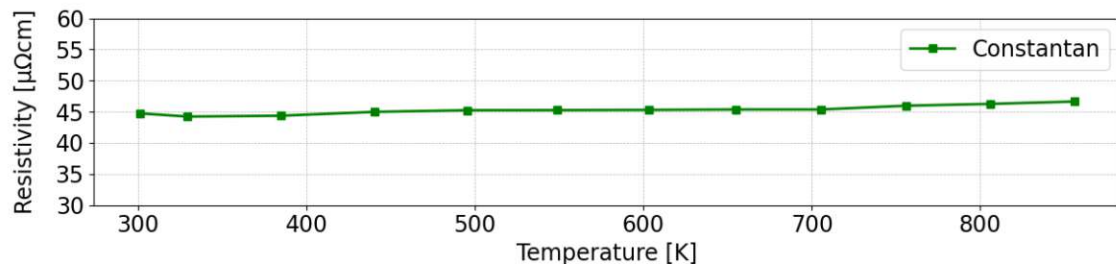
Figure 28: ULVAC ZEM-3 resistivity measurement results of Constantan as function of temperature.

5.2.2   Bismuth

Already in their original publication [5] Nernst and Ettinghausen reported that bismuth showed by far the highest measured Nernst coefficient compared to other elemental materials such as nickel, cobalt, iron and antimony. Bismuth is a semimetal, which has a crystal structure based on the rhombohedral lattice with two atoms per unit cell [23, 24]. As bismuth is the element with the highest known Nernst coefficient [25], it was the first sample chosen to verify the functionality of the measurement setup to correctly detect the Nernst coefficent of a sample.

For polycrystalline bismuth, several different values of the Seebeck- and Nernst coefficients have been reported for temperatures around room temperature over the years, which are summed up in table 3 and 4. Unfortunately, none of these references report data for temperatures above room temperature.

Reported values of the Seebeck coefficient of polycrystalline bismuth				
Ref.	Year	Temperature [K]	Value [µV/K]	Field dependency [µV/K]
[26]	2003	290K	-59	-110 at 5T
[27]	2006	300K	-60	not reported
[28]	2018	300K	-61.5	not reported
[29]	2020	300K	-75	-90 at 0.5T

Table 3: Reported values of the Seebeck coefficient of of polycrystalline bismuth close to room temperature.

Reported values of the Nernst coefficient of polycrystalline bismuth				
Ref.	Year	Fieldrange [T]	Temperature [K]	Max. value [µV/KT]
[30]	1992	0 to 1.2	275	10
[26]	2003	-5 to +5	200/290	100.5/17.4
[28]	2018	-0.3 to 0.3	300	18.3
[29]	2020	0.5 (single)	250	16

Table 4: Reported values of the Nernst coefficient of polycrystalline bismuth.

Figure 29 shows the measurement results of the Seebeck coefficient and its dependence on magnetic fields as well as resistivity measurement results. The Seebeck coefficient shows a slight quadratic dependence on the magnetic field that was also previously observed for bismuth single crystals [31, 32] and becomes more prominent with increasing temperature. Figure 30 displays the resistivity measurement results, showing a slight but noticeable T^2 dependence that was first discussed by Hartman in 1969 [33] and attributed to electron-electron scattering. The T^2 dependence of the resistivity of materials such as bismuth, graphite, UPt_3 and Sr_2RuO_4, that is highly suppressed for conventional metals, is still a current topic of research [34].
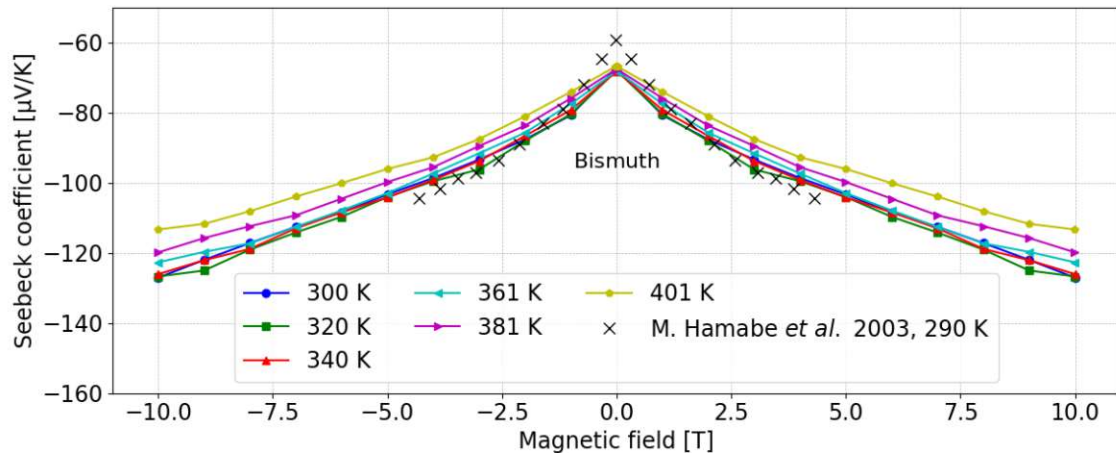
Figure 29: Seebeck coefficient of bismuth as a function of the magnetic field for different temperatures.
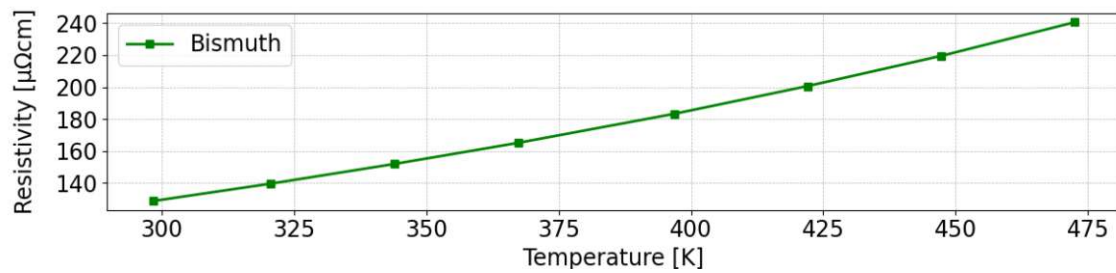

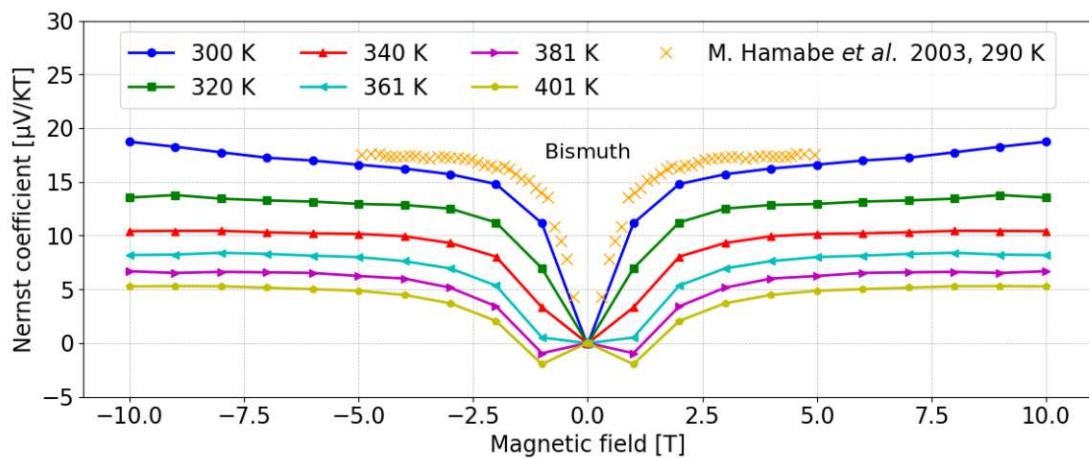Figure 30: Resistivity of bismuth as function of temperature.

Figure 31: Measurement results for the Nernst coefficient of bismuth as a function of the magnetic field for different temperatures.
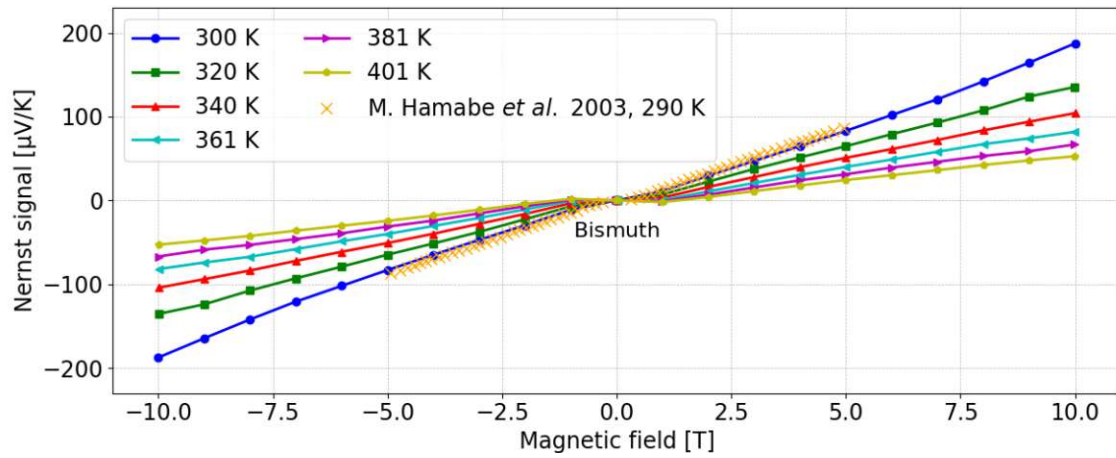
Figure 32: Measurement results for the Nernst signal of bismuth as a function of the magnetic field for different temperatures.
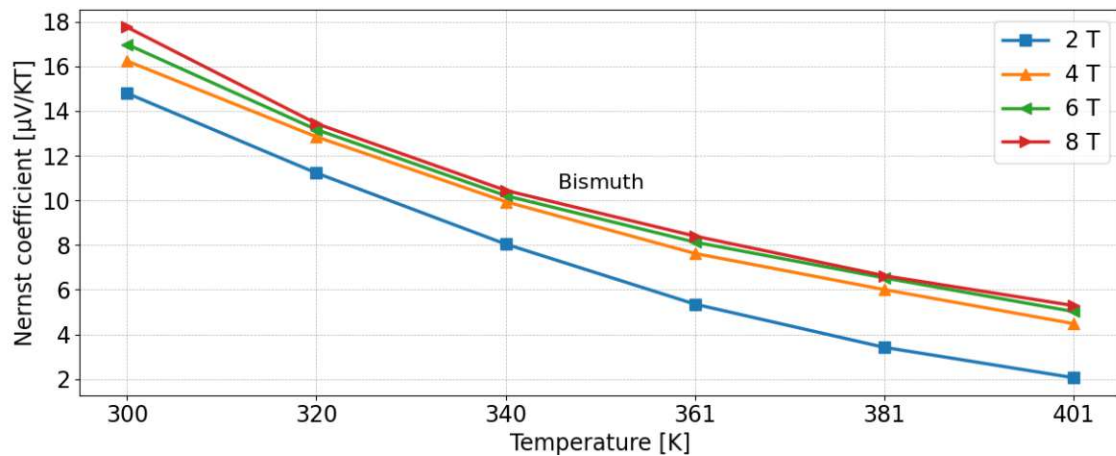

Figure 33: Temperature dependence of the Nernst coefficient of bismuth for different values of the magnetic field.

Figure 31 shows the measured values for the Nernst coefficient reaching maximum values around 18 µV/KT, which is in excellent agreement with the reported values from 2003 and 2018 at around room temperature. The observed sign reversal of the Nernst coefficient at low magnetic fields that becomes more defined with increasing temperatures, was also previously reported for both single crystal and polycrystalline samples [30, 35]. Figure 32 shows the product of the Nernst coefficient and magnetic field, introduced as Nernst signal in equation (5) which is a more practical way to plot and discuss the Nernst coefficient, as it has the same units, µV/K, as the Seebeck coefficient. The decrease of the Nernst coefficient with increasing temperature is explicitly displayed in Figure 33, confirming the observations of Ref.[26].

5.2.3 $Co_2MnAl_{1-x}Si_x$ Heusler alloys

To verify the capability of the measurement system to detect the anomalous Nernst Effect, it was decided to synthesize and measure the Heusler alloy $Co_2MnAl_{0.63}Si_{0.37}$. As reported in Ref.[8], Co_2MnAl has been predicted to have Weyl points near the Fermi level in the $L2_1$-ordered structure, which is expected to give rise to exotic transverse transport properties such as large anomalous Nernst effect due to a large Berry curvature. The study revealed that Al/Si substitution shifts the position of the Fermi level and greatly improves the $L2_1$ atomic ordering, leading to strong enhancement of the anomalous Nernst effect. It was also shown that higher annealing temperatures increase the $L2_1$ ordering. The highest value of the Nernst signal, 5.7 µV/K, was reported for 30 nm single crystal films of $Co_2MnAl_{0.63}Si_{0.37}$ annealed at 700°C and measured at room temperature. For the same sample annealed at 500°C a maximum value of about 2.2 µV/K was reported.
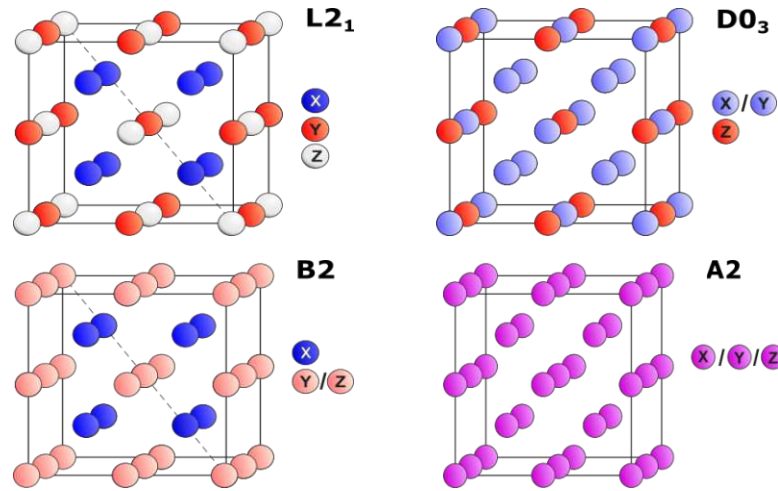

Figure 34: Crystal structures of X_2YZ Heusler alloys.

The polycrystalline bulk sample of $Co_2MnAl_{0.63}Si_{0.37}$ synthesized for this diploma thesis was annealed at 900°C. It shows medium levels of L_{21} ordering. This is indicated by the existence of the (111) and (200) peak while comparing the XRD measurement data and theoretical data obtained from the Rietveld refinement, shown in 35. The experimental lattice parameter a=5.723 Å, obtained from refinement, lies well between the literature values of 5.755 and 5.654 Å for Co_2MnAl and Co_2MnSi, respectively [36]. The Seebeck coefficient of $Co_2MnAl_{0.63}Si_{0.37}$ is negative and decreases with temperature as shown in Figure 36. Figure 37 shows the dependence of the Seebeck coefficient on the magnetic field. Compared to the results of bismuth, the dependence saturates at magnetic fields above 1 Tesla for all temperatures and is very subtle overall. The resistivity measurement data, shown in Figure 38, displays a slight T^2 dependence on temperature that was also previously reported for Co_2MnAl [37].
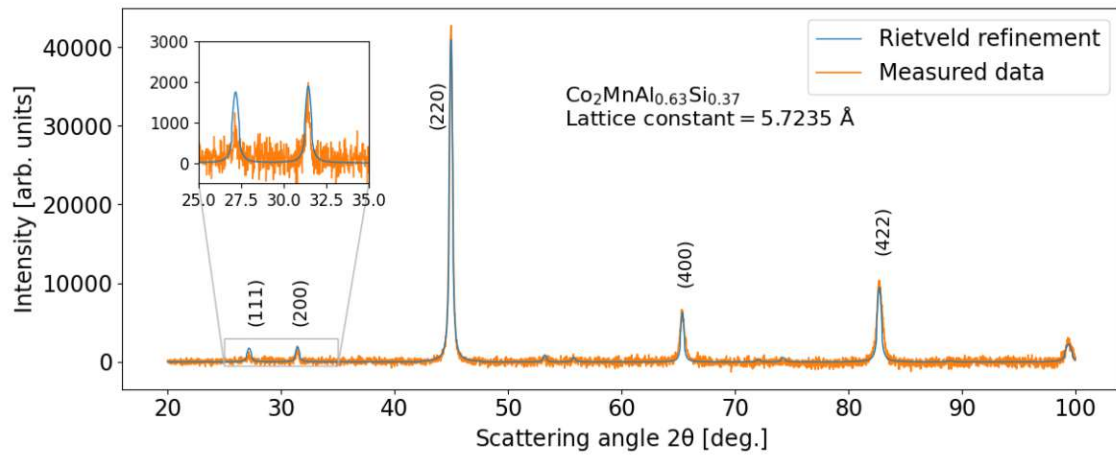
Figure 35: XRD measurement results of $Co_2MnAl_{0.63}Si_{0.37}$. $L2_1$ ordering is indicated by the existence of the (111) and (200) peak.

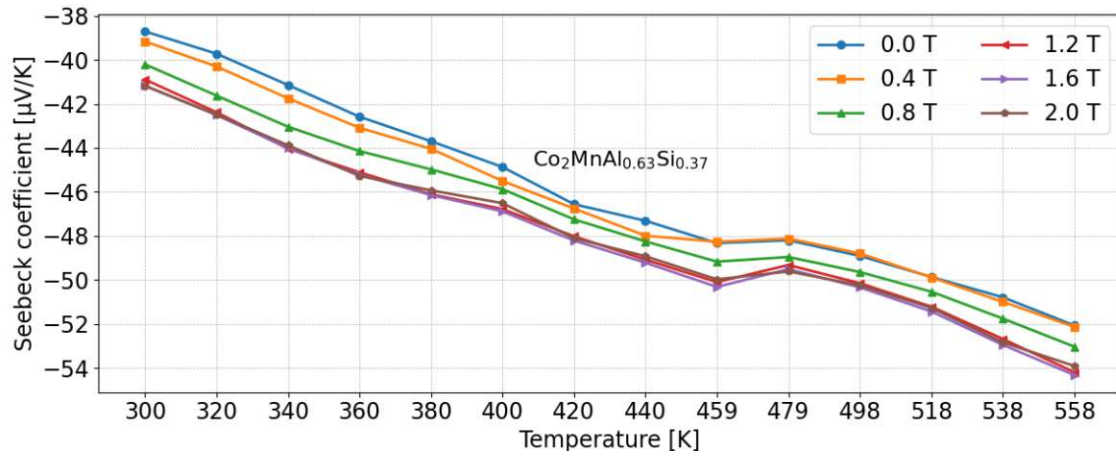Figure 36: Seebeck coefficient measurement results of $Co_2MnAl_{0.63}Si_{0.37}$ as function of temperature for different values of the magnetic field.
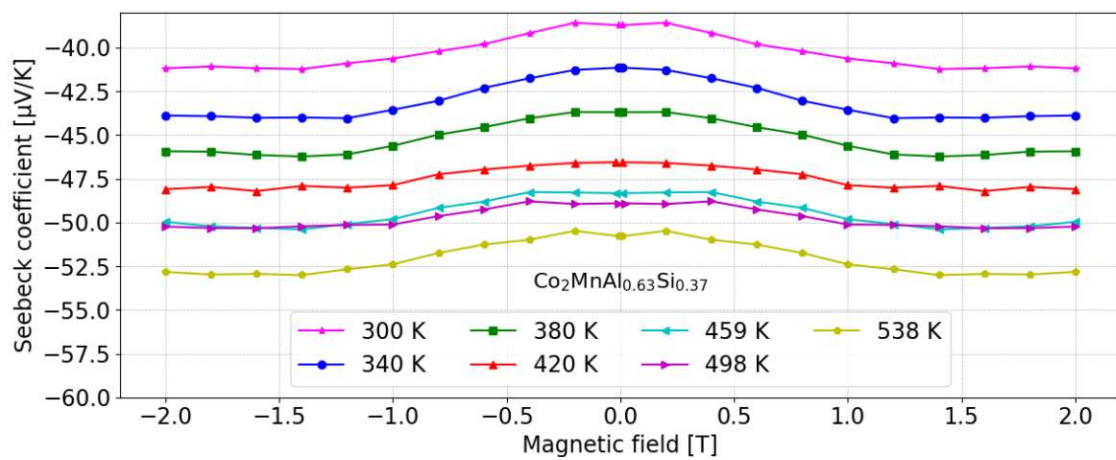

Figure 37: Seebeck coefficient measurement results of $Co_2MnAl_{0.63}Si_{0.37}$ as function of the magnetic field for different values of temperature.
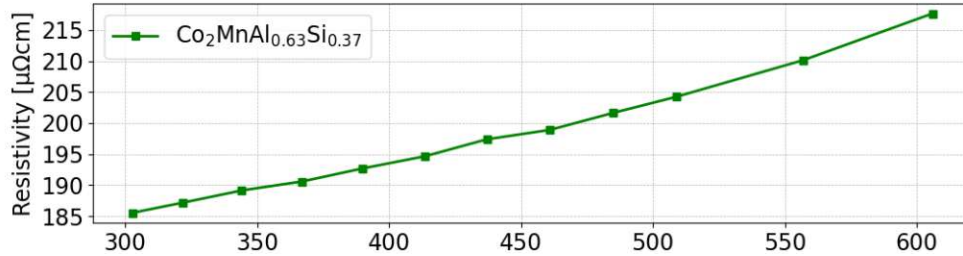
Figure 38: ULVAC ZEM 3 resistivity measurement results of $Co_2MnAl_{0.63}Si_{0.37}$ as function of temperature.
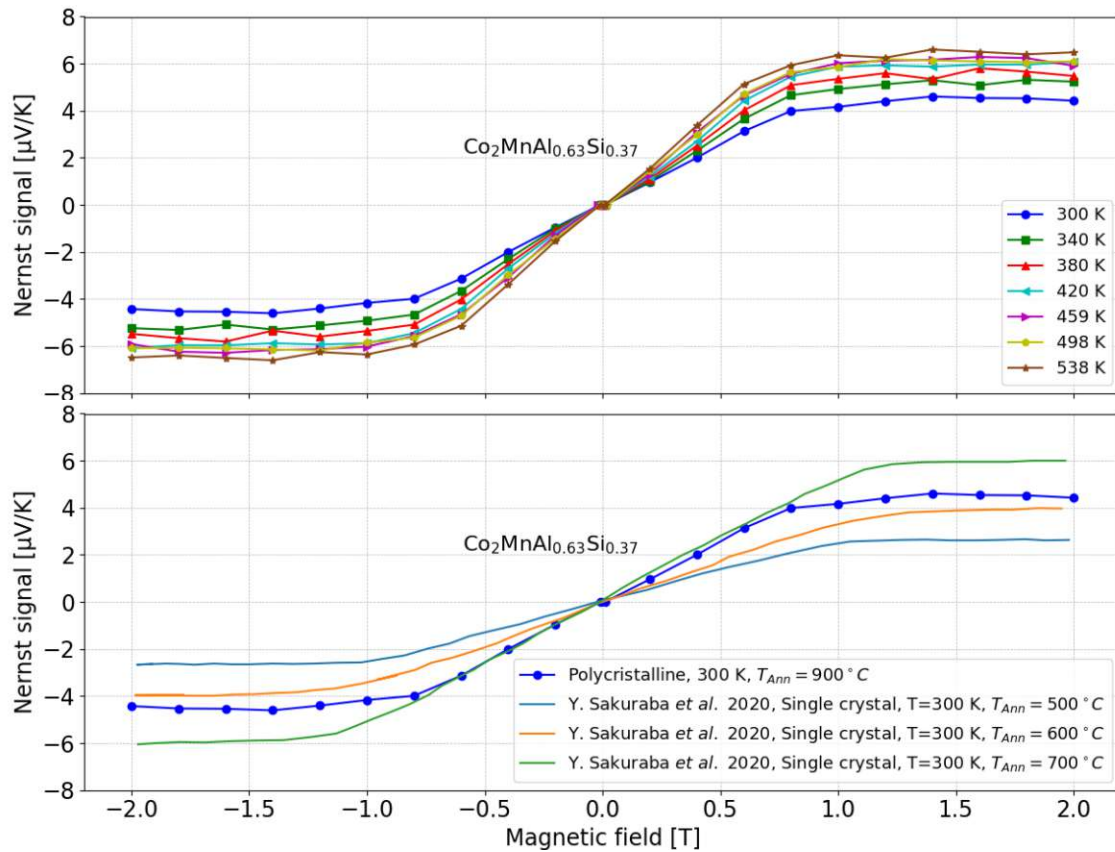

Figure 39: (Top) Nernst signal measurement results of $Co_2MnAl_{0.63}Si_{0.37}$ as a function of the magnetic field for different values of temperature. (Bottom) Nernst signal measurement results of $Co_2MnAl_{0.63}Si_{0.37}$ compared with reference data 40.

Figure 39 shows the measurement results for the Nernst signal as function of the magnetic field for various temperatures. At room temperature the value of the Nernst signal saturates at 1 T and at about 4 µV/K. The maximum value of about 6.1 µV/K is reached at the highest measured temperature at around 540 K. Additionally, the measurement values are compared with the reported values of Ref. [8] showing similar results in magnitude and shape of the Nernst signal, although polycrystalline samples annealed at a higher temperature were measured as opposed to single crystal films. The temperature dependence of the Nernst signal, displayed in detail in Figure 40 for low magnetic fields, confirms a linear-like increase of the Nernst signal with temperature that was also observed for other ferromagnetic Heusler compounds in Ref. [38].
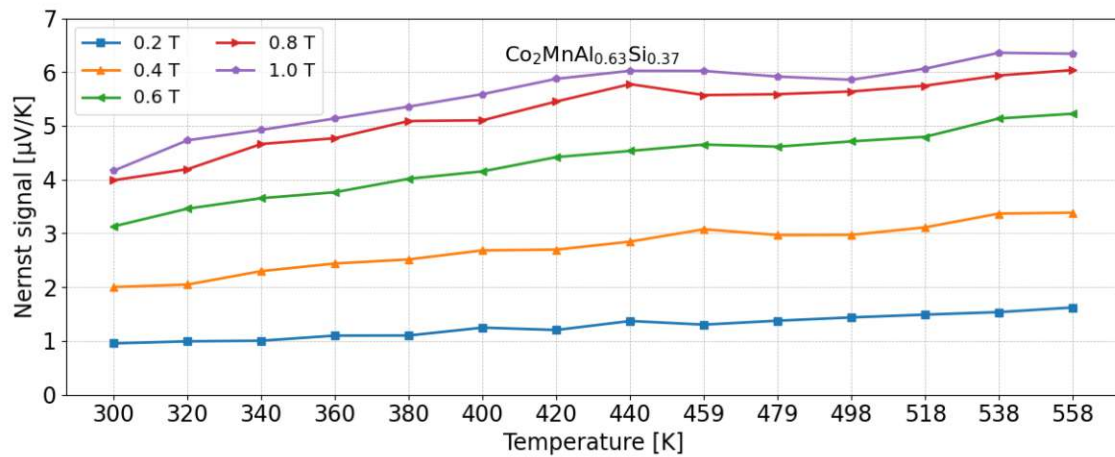

Figure 40: Temperature dependence of the Nernst signal of $Co_2MnAl_{0.63}Si_{0.37}$. A slight increase with temperature can be observed.

5.2.4   Fe$_2$ based Heusler alloys

The anomalous Nernst effect has also recently been studied for various Fe-based Heusler compounds Fe$_2$YZ (Y = Co, Ni; Z = Al/Ga)[38]. Similar to Co$_2$MnAl$_{0.63}$Si$_{0.37}$ the large intrinsic Berry curvature is responsible for the large anomalous Nernst effect in these compounds. Fe$_2$CoAl and Fe$_2$NiAl were chosen to be synthesized for comparison with the published results. Additionally, Fe$_2$CoAl$_{0.5}$Si$_{0.5}$ was synthesized and measured as a blind guess. It is again to note that single crystals, grown using the Bridgeman method, were used for the measurements in Ref. [38], while the samples synthesized for this diploma thesis are again polycrystalline bulk samples. In addition, the synthesized samples were measured without annealing compared to a 14 day annealing cycle for the samples in Ref. [38] at 600°C and 900°C for Fe$_2$CoAl and Fe$_2$NiAl, respectively.
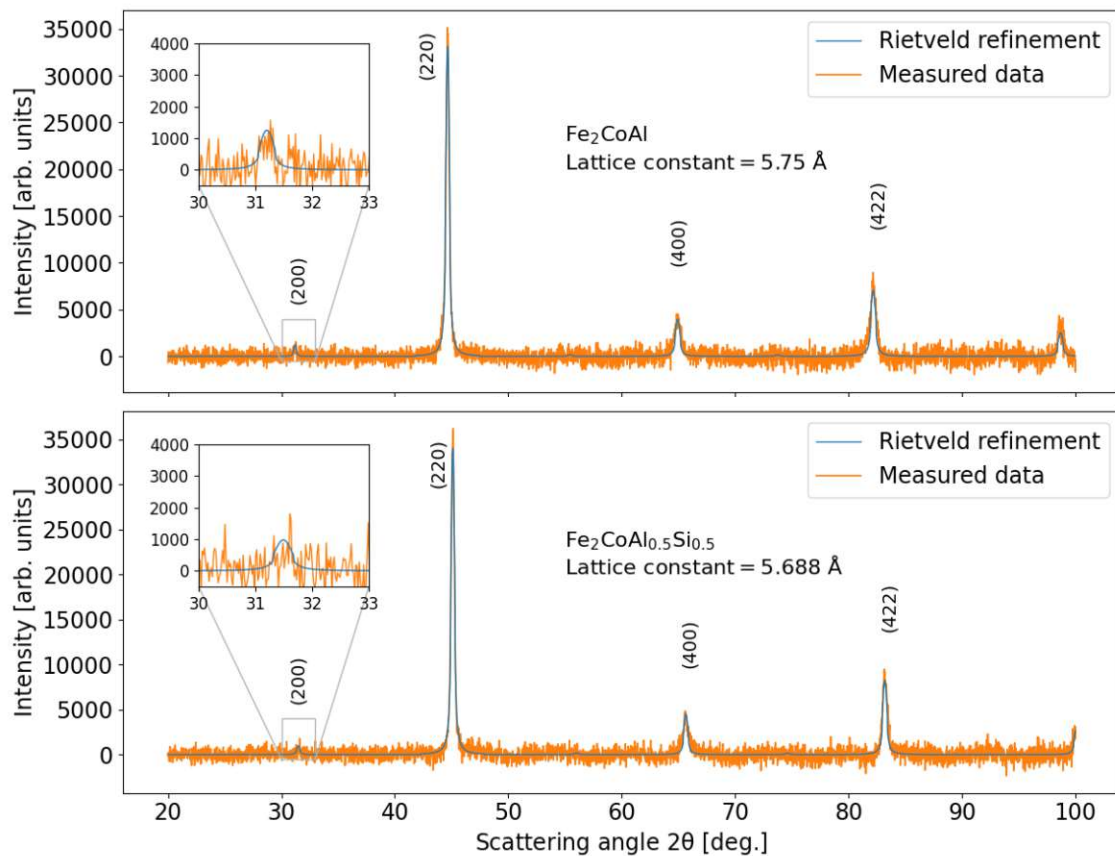

Figure 41: (Top) XRD measurement results of Fe$_2$CoAl. (Bottom) XRD measurement results of Fe$_2$CoAl$_{0.5}$Si$_{0.5}$. The missing (111) peak for both samples indicates B2-type disordering.

The XRD measurement data of Fe$_2$CoAl and Fe$_2$CoAl$_{0.5}$Si$_{0.5}$ presented in Figure 41 does not show the (111) peak and only a small (200) peak, indicating B2-type disorder, which was also reported for polycrystalline Fe$_2$YZ samples in [38, 39, 40, 41].

Unfortunately, the X-ray diffraction measurement data of Fe_2NiAl displays high levels of distortion and could not be fit to a calculated crystal. It is assumed that this is the case, because Fe_2NiAl is much more ductile than the other sample. Therefore, it was difficult to achieve the same fineness of powder from crushing the sample required for better resolution of the measurement data. The Seebeck coefficient of
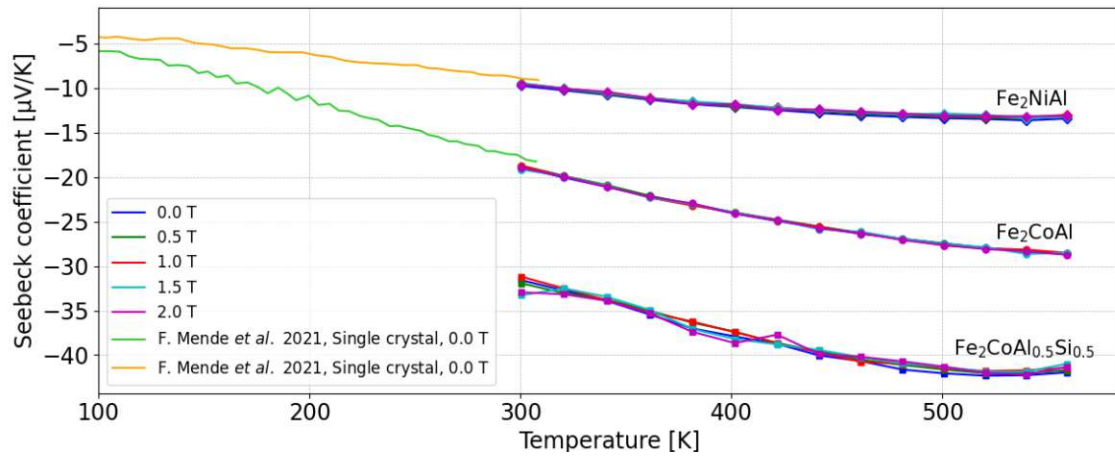

Figure 42: Seebeck coefficient measurement results of Fe_2 based Heusler alloys as function of temperature for different values of the magnetic field.
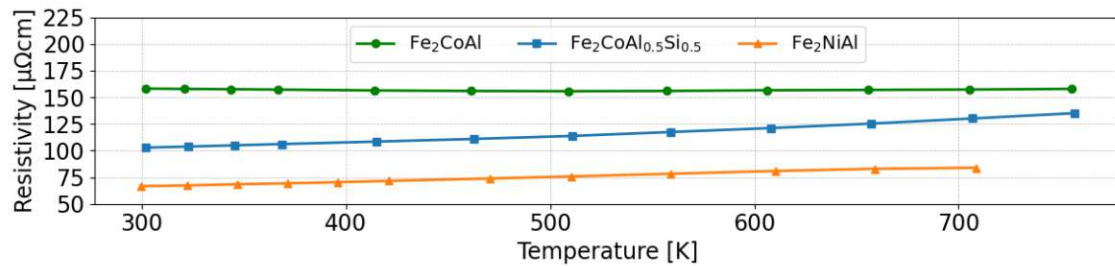

Figure 43: ULVAC ZEM 3 resistivity measurement results as function of temperature.

all compounds is negative and increases with temperature as shown in Figure 42. The combination with the low temperature measurement results reported in [38], shows excellent agreement. The data show no magnetic field dependence of the Seebeck coefficients. $Fe_2CoAl_{0.5}Si_{0.5}$ shows a higher signal-to-noise ratio as compared to the other two samples. As shown in Figure 43, the resistivity of Fe_2CoAl remains almost constant over the temperature range while $Fe_2CoAl_{0.5}Si_{0.5}$ and Fe_2NiAl show slightly increasing values with temperature. Figure 44 exhibits the Nernst signal measurement results individually and compared with the published results, showing excellent agreement for Fe_2CoAl and good agreement for Fe_2NiAl. As reported in Ref. [38], the Nernst signal of the Fe_2YZ samples increases linearly with temperature, which can be confirmed looking, at the respective measurement data for Fe_2CoAl and and $Fe_2CoAl_{0.5}Si_{0.5}$ shown in Figure 44.

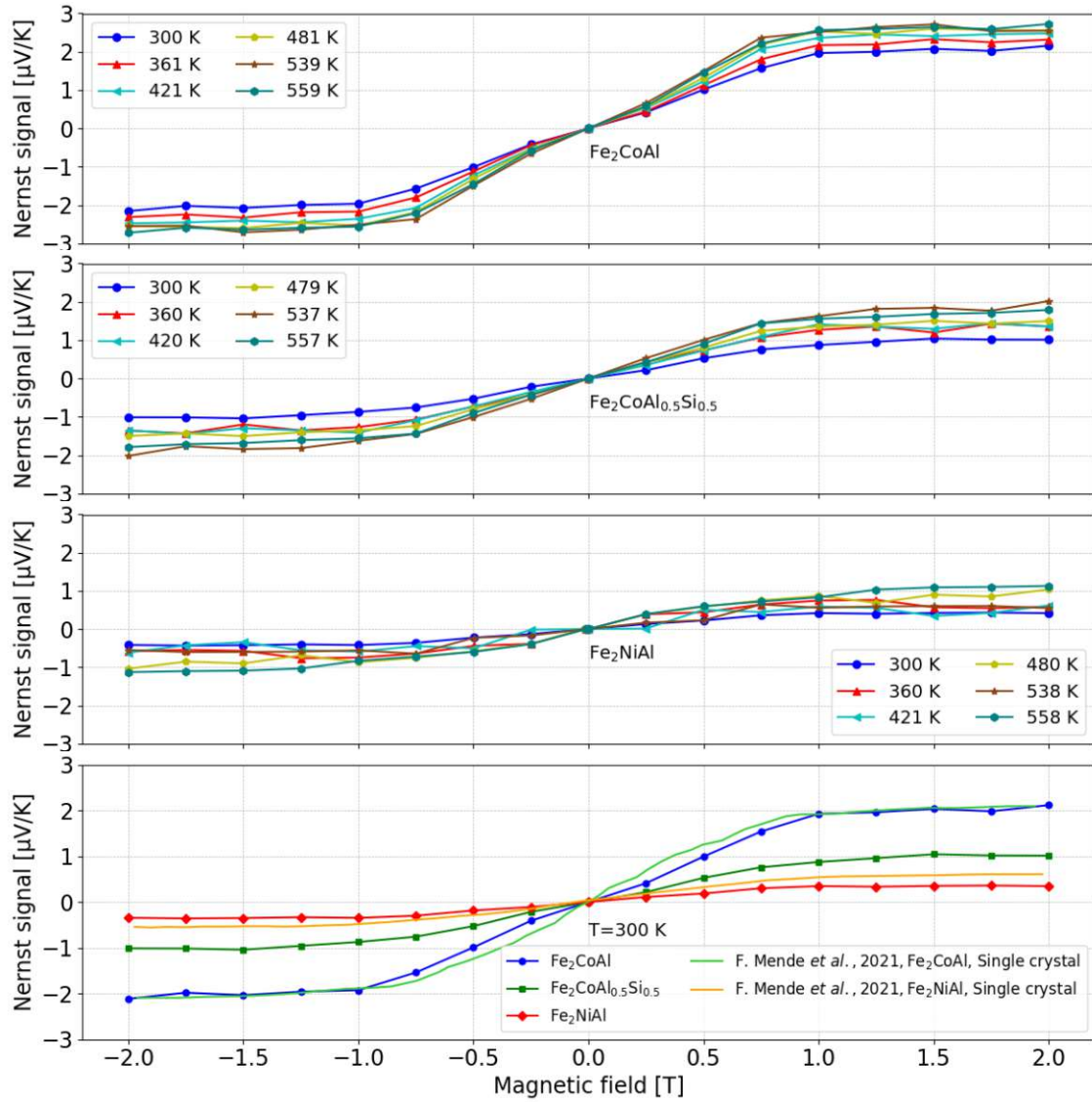Figure 44: (Top, Middle) Nernst signal measurement results of Fe_2CoAl, $Fe_2CoAl_{0.5}Si_{0.5}$, Fe_2NiAl as function of magnetic field for different values of temperature.(Bottom) Nernst signal measurement results of Fe_2CoAl compared with reference data.

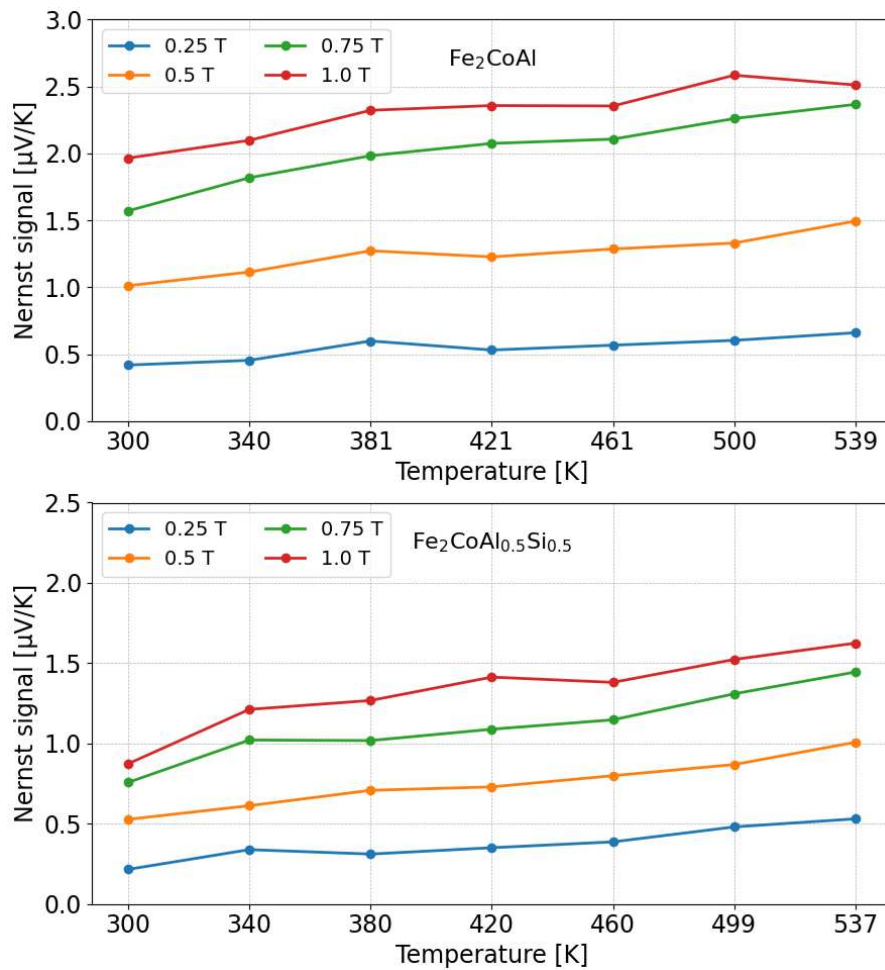Figure 45: (Top) Temperature dependence of the Nernst signal of Fe_2CoAl. (Bottom) Temperature dependence of the Nernst signal of $Fe_2CoAl_{0.5}Si_{0.5}$. A slight increase with temperature can be observed for both samples.

5.2.5 Fe₃ based alloys

Another very recent publication [42] provides detailed theoretical and experimental results for the anomalous Nernst effect of Fe_3X (X=Al/Ga) single crystal thin films. It is shown that substituting 25 percent of alpha iron with aluminium or gallium, dramatically increases the anomalous Nernst Effect by one order of magnitude compared to undoped alpha iron. The difference between applying the temperature gradient in plane or out of plane with the crystal structure was also studied. The reported maximum value of the Nernst signal of Fe_3Al at room temperature is around 2 µV/K and 4 µV/K for an applied temperature gradient in and out of plane of the single crystal film, respectively. To investigate these results Fe_3Al was chosen to be synthesized, while $Fe_3Al_{0.5}Si_{0.5}$ was synthesized to investigate the effect of Si-doping in this compound.

The crystal structure of Fe_3Al is reported to be either a DO_3 type ordered structure, partially disordered B_2 type, or fully disordered A_2 type [42]. The XRD measurement data displayed in Figure 46 show an absence of the (111) and (200) peaks for Fe_3Al, which is characteristic of the fully disordered A_2-type structure. The lattice parameter a=5.810 Å is close to the reported value of a=5.79 Å from Ref. [42]. Similar to Fe_2NiAl, it was not possible to achieve a similar fineness of powder due to the high ductility of the Fe_3 based alloys. The resulting additional distortion in the measurement is assumed to be the cause of the wider peak width and incorrect peak height when compared to Rietveld refinements of the theoretical structure. This could also be the cause of the missing (111) and (200) peaks in the Fe_3Al sample. The Rietveld refinement of the $Fe_3Al_{0.5}Si_{0.5}$ data indicates B_2 type disorder as the (111) peak is present.
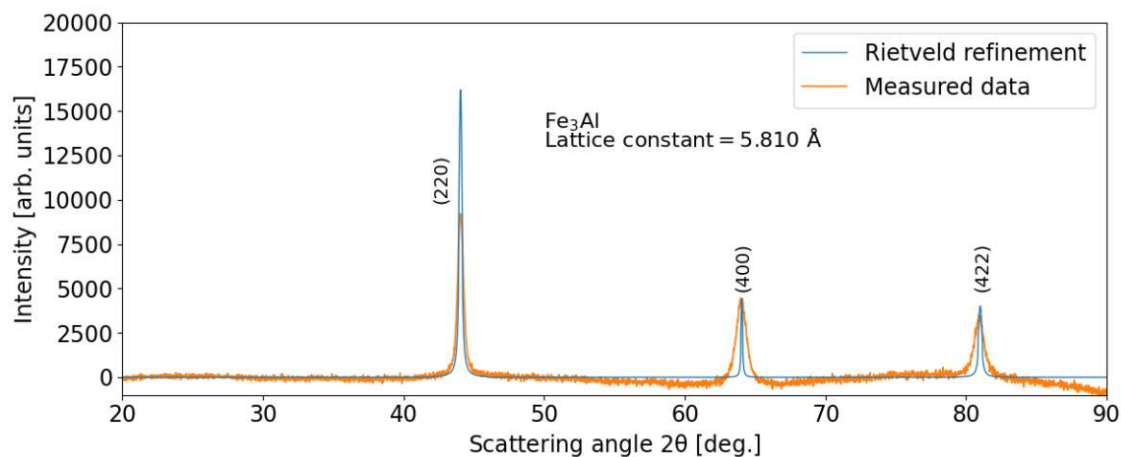

Figure 46: XRD measurement results of Fe_3Al. A2-type disordering is indicated based on the absence of the (111) and (200) peak. The distortion of the measurement data is presumably due to the inability to create fine powder of Fe_3Al.
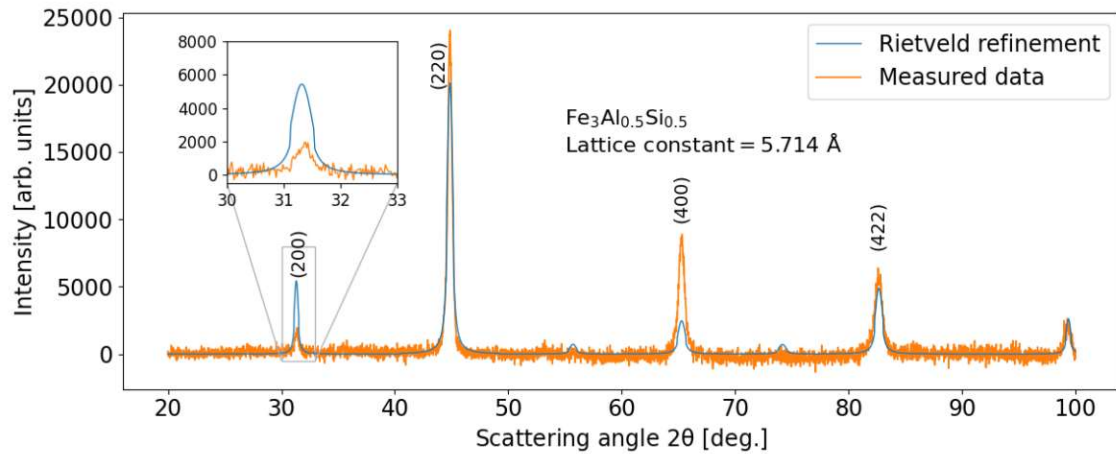
Figure 47: XRD measurement results of $Fe_3Al_{0.5}Si_{0.5}$. B2-type disordering is indicated based on the absence of the (111) peak. The distortion of the measurement data is presumably due to the inability to create fine powder of $Fe_3Al_{0.5}Si_{0.5}$.

As shown in Figure 48, the Seebeck coefficient of both Fe_3Al and $Fe_3Al_{0.5}Si_{0.5}$ is negative and decreases with temperature. The comparison with the published results of [42] is in reasonable agreement. Unfortunately, no further experimental results were found to confirm the decreasing behaviour of the Seebeck coefficient of Fe_3Al above 400 K. Figure 49 shows the resistivity measurements, which are in excellent agreement with the published results for Fe_3Al. Figures 50a-c show the Nernst signal measurement results individually and compared with the published results. The Fe_3Al measured in Ref. [42] shows in-plane magnetization with a coercive field B_c of about 20 Oe, which yields a Nernst signal at zero field for the out-of-plane temperature gradient.
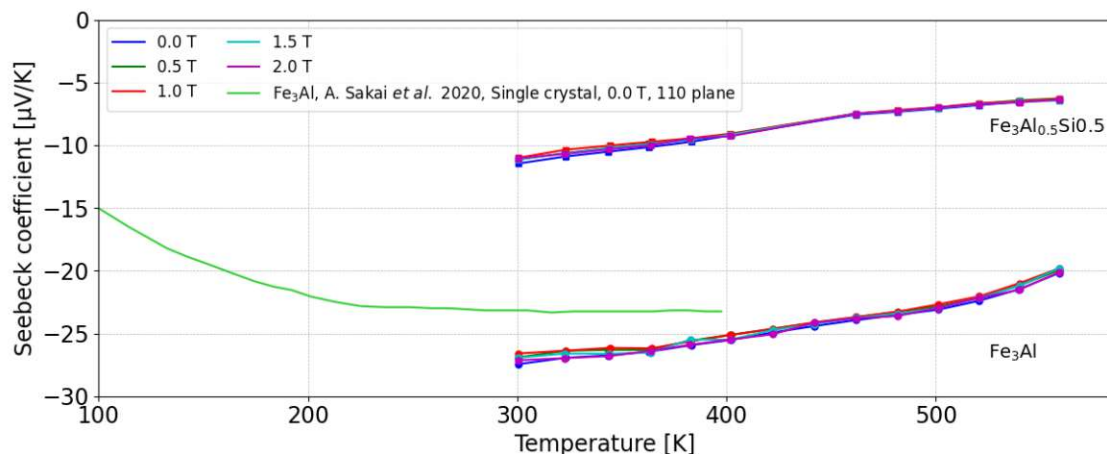
Figure 48: Seebeck coefficient measurement results of Fe_3 based Heusler alloys as function of temperature for different values of magnetic field.
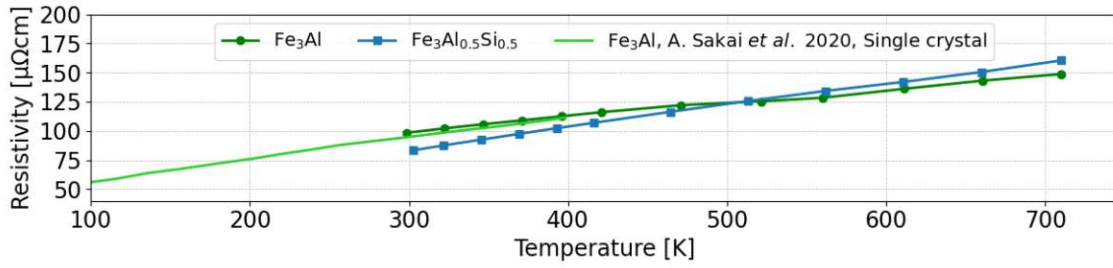
Figure 49: ULVAC ZEM 3 resistivity measurement results as function of temperature.
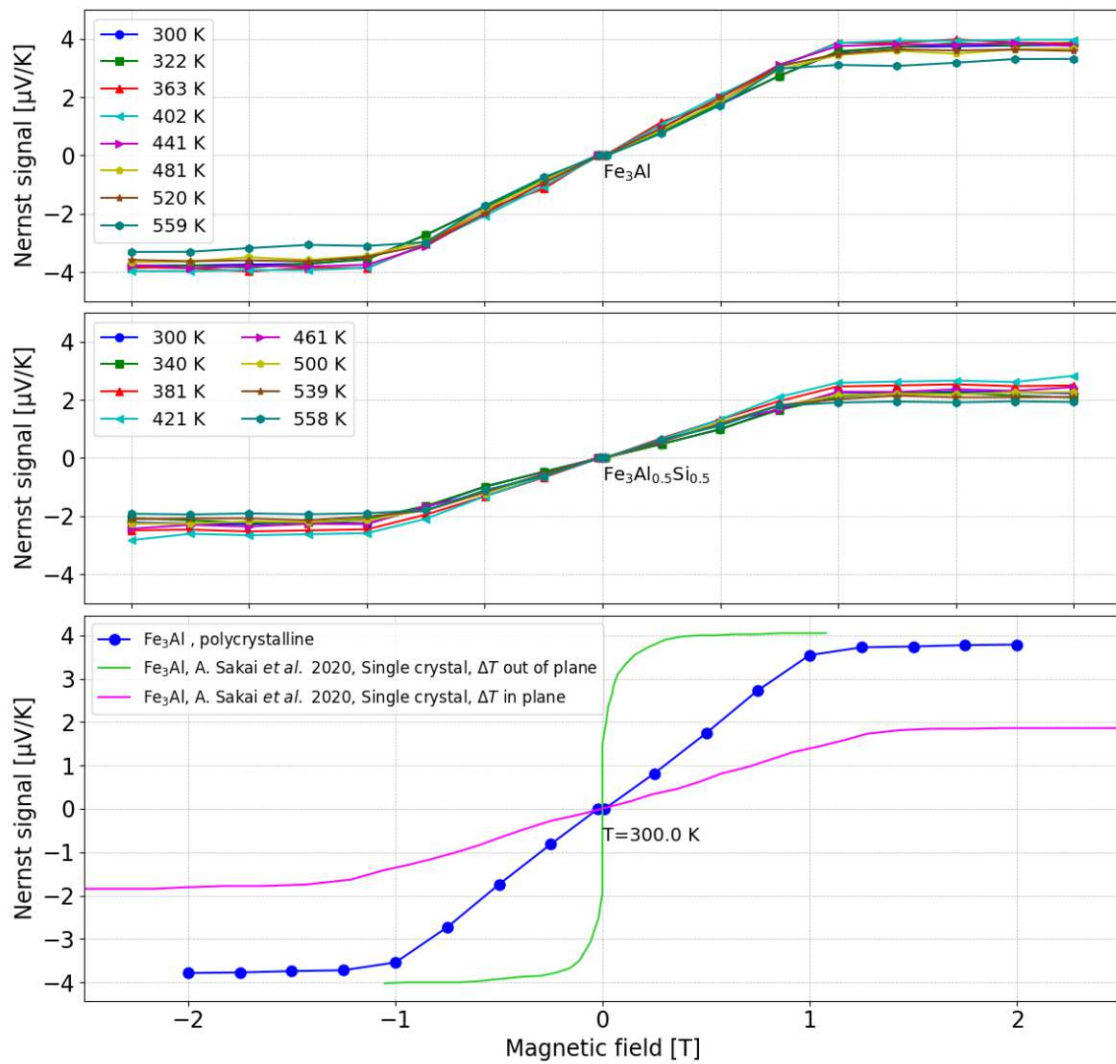
Figure 50: (Top,Middle) Nernst signal measurement results of Fe_3Al and $Fe_3Al_{0.5}Si_{0.5}$ as a function of the magnetic field for different values of temperature. (Bottom) Nernst signal measurement results of Fe_3Al compared with reference data for 300 K.

Displayed in Figure 50, the Nernst signal measurement results of the Fe_3Al sample snythesized for this diploma thesis, show excellent agreement with the reported maximum value of 4 µV/K. However, due to the lack of a coercive field the maximum value is reached at 1 Tesla. The Nernst signal of $Fe_3Al_{0.5}Si_{0.5}$ shown in Figure 50 reaches a maximum of around 2.5 µV/K. Displayed in Figure 51, both samples do not show an increase of the Nernst signal with increasing temperature. This observation is in good agreement with the temperature dependence shown in Ref.[42] for temperatures above 300 K.

Figure 51: (Top) Temperature dependence of the Nernst signal of Fe_3Al. (Bottom) Temperature dependence of the Nernst signal of $Fe_3Al_{0.5}Si_{0.5}$.

5.3   Comparison and summary of measurement results

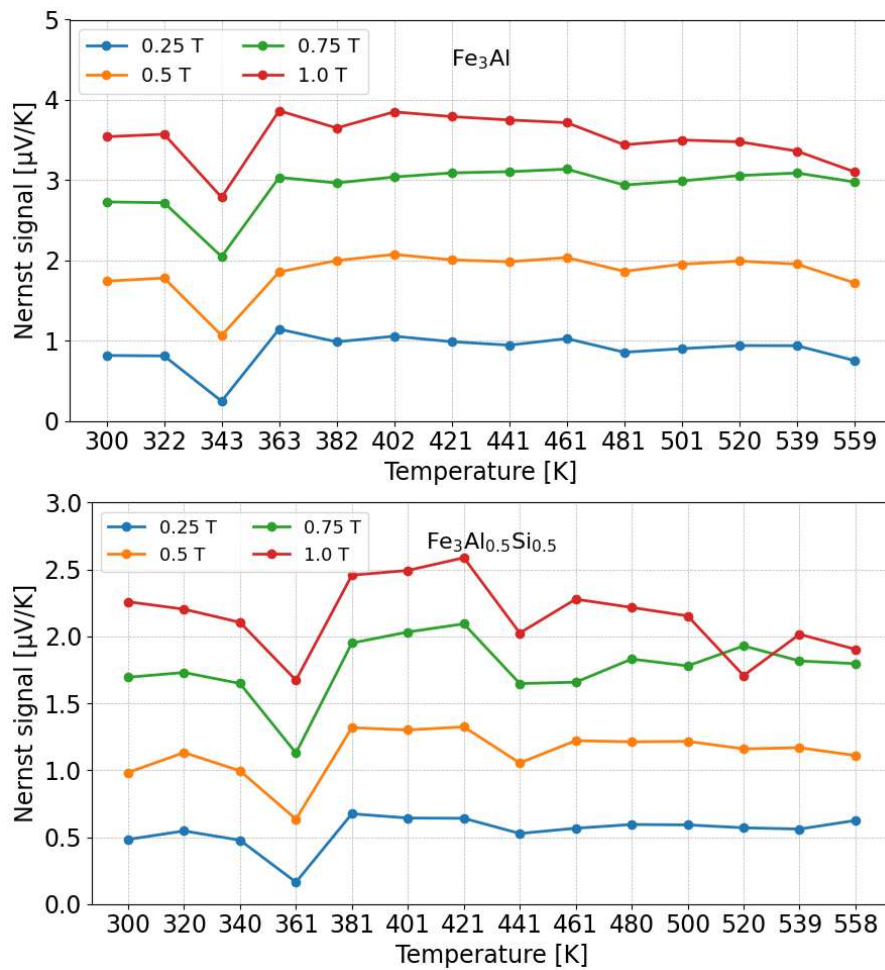The temperature-dependent resistivity of all samples is shown in Figure 52. Compared to the metallic samples, which exhibit the expected linear temperature-dependence at high temperatures, the T^2 dependence can clearly be observed for the semimetal bismuth and Weyl semimetal $Co_2MnAl_{0.63}Si_{0.37}$. Also, the constant resistivity behaviour of Constantan is visible, as well as Fe_2CoAl barely showing any temperature dependence in the resistivity.
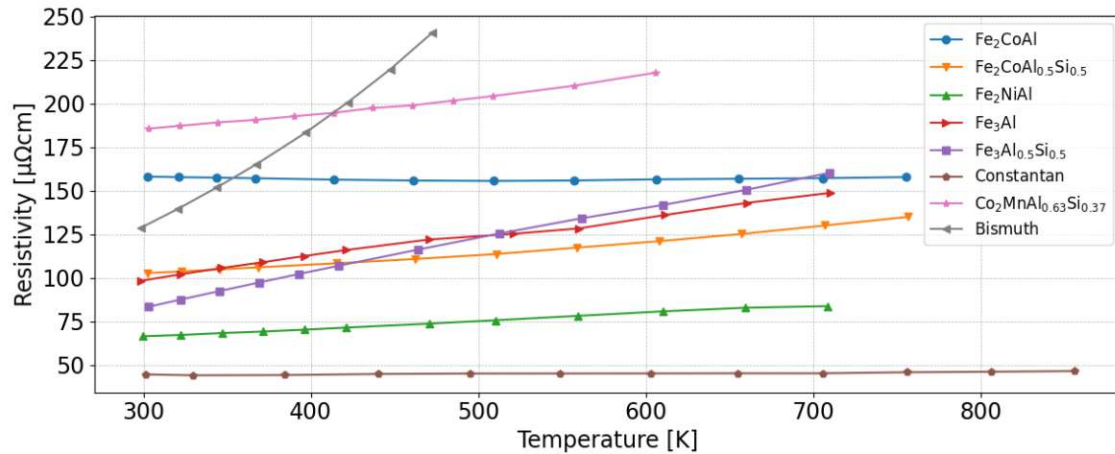
Figure 52: Comparison of the ULVAC ZEM 3 resistivity measurements as function of temperature of all samples. The T^2 dependence can clearly be observed for the semimetal bismuth and Weyl semimetal $Co_2MnAl_{0.63}Si_{0.37}$.

As summarized in Figure 53, the Seebeck coefficient of all measured samples is negative, indicating electrons as dominant charge carriers of the respective materials. Substitution of aluminium by silicon for Fe_2CoAl and Fe_3Al has a significant impact on the magnitude of the Seebeck coefficient, whereas the temperature dependence remains similar. As already mentioned in section 2.1, the existence of a magnetic field dependence of the Seebeck coefficient is always accompanied by the Nernst effect and vice versa. While this observation does hold true for the conventional Nernst- and Seebeck effect in bismuth, it was also observed for $Co_2MnAl_{0.63}Si_{0.37}$, as shown in Figure 54. For the other samples, exhibiting the anomalous Nernst effect, a clear dependence of the Seebeck coefficient on the magnetic field could not be observed.
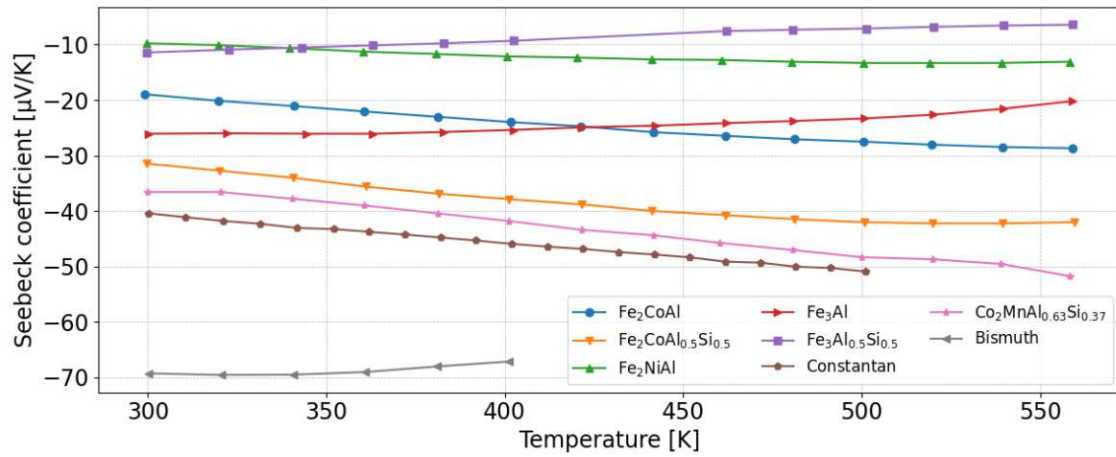
Figure 53: Comparison of the Seebeck coefficient measurement results of all samples as function of temperature.
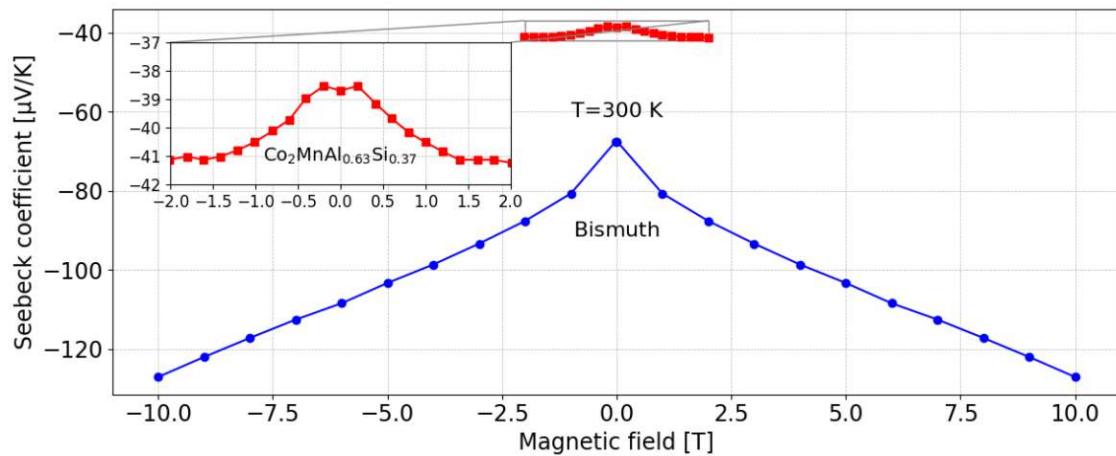
Figure 54: Comparison of the Seebeck coefficient measurement results at room temperature for bismuth and $Co_2MnAl_{0.63}Si_{0.37}$ as function of the magnetic field. For the other samples, that exhibit the anomalous Nernst effect, a clear dependence of the Seebeck coefficient on the magnetic field could not be observed

Inspecting Figure 55, the difference between the conventional Nernst effect and anomalous Nernst effect is obvious. While the signal of the conventional Nernst effect shows strictly linear dependence on the magnetic field, the shape of the anomalous Nernst effect is reminiscent of a ferromagnetic magnetization curve, suggesting the correlation of the anomalous Nernst effect to ferromagnetism, as expressed by the emperical equation (4). Analogous to the Seebeck coefficient, the substitution of aluminium with silicon for Fe_2CoAl and Fe_3Al has a significant impact on the magnitude of the Nernst signal.
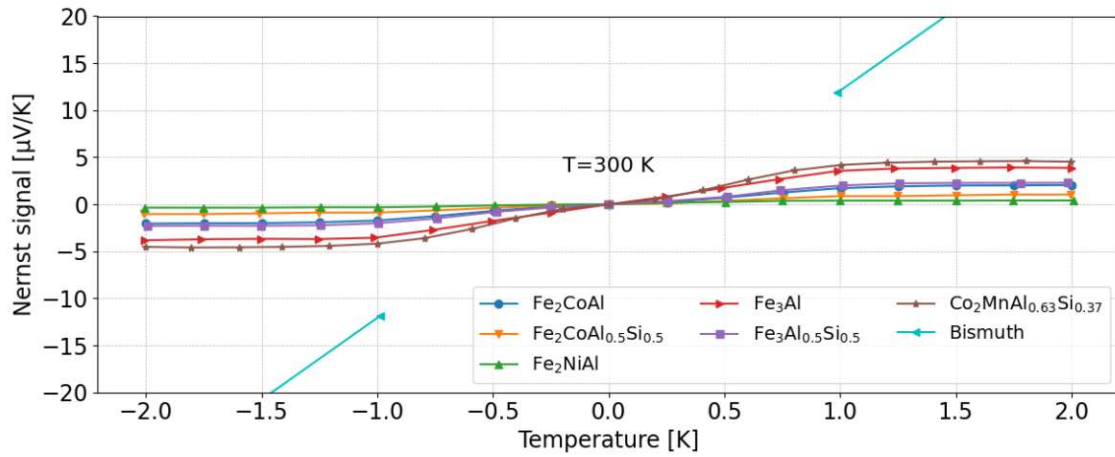
Figure 55: Comparison of the Nernst signal measurement results at room temperature of all samples. While the signal of the conventional Nernst effect (bismuth) shows strictly linear dependence on the magnetic field, the shape of the anomalous Nernst effect is reminiscent of a ferromagnetic magnetization curve, suggesting the correlation of the anomalous Nernst effect to ferromagnetism as expressed by the empirical equation (4).

6   Conclusion

In this work the Seebeck- and Nernst effect at high temperatures and high magnetic fields were studied. Using the phenomenological expressions for both phenomena a model setup was designed. Based on it, a measurement setup was created that was tested for simultaneous measurements of both coefficients between room temperature and 560 K, as well as magnetic fields up to 10 Tesla. To control and monitor the measurements, a designated measurement software and user-friendly graphical interface was designed and implemented. For all measurements, apart from Constantan, polycrystalline bulk samples were synthesized, using a high frequency induction melting system at IFP.

Overall, the measurement results are in excellent agreement with published reference data for both the Seebeck- and the Nernst coefficient. The measurement setups performance is reliable, consistent and does not show any deviations in data quality or noise level, when tested for various different samples. For Nernst signals around and below 0.5 µV/K the performance is affected by noise and the shape of the signal becomes less consistent. Nonetheless, signals in this range can still be identified, having physical origin such as the anomalous Nernst effect.

Apart from the reference measurements using Constantan and bismuth, the comparison of the results for cobalt and iron based Heusler alloys revealed that the magnitude of the anomalous Nernst effect is remarkably consistent for polycrystalline bulk samples and single crystal thin films. Apart from the samples that were compared with literature values, $Fe_2CoAl_{0.5}Si_{0.5}$ and $Fe_3Al_{0.5}Si_{0.5}$ performed as expected, showing a significant impact on the magnitude of the Nernst- and Seebeck effect due to the respective substitution of aluminium by silicon.

7 Outlook

Even though the performance of the measurement setup is excellent, there are several aspects that could be improved and expanded for future use and flexibility.

- **Reducing noise resulting from spurious voltages at contact points**: Due to the nature of the Seebeck effect thermoelectric voltages occur at any kind of contact point of two materials given a temperature difference between them. Although the measurement equations (53) and (54) eradicate constant spurious offset voltages during measurements, they can still be affected by changing temperature differences during measurements at any contact point of the circuit. Currently, the copper wires for the Nernst measurements as well as the R-type thermocouple are connected by soldering points inside and outside of the Fischer connector of the sample holder respectively. Additionally, the copper cables leading from the sample holder is contacted to the respective nanovoltmeter by solder. To minimize the noise created by temperature changes at the contact points, it might help to entirely abandon solder contacts along the signal paths.

- **Improving the maximum temperature of the sample holder**: The maximum base temperature of the sample holder was set to 560 K for this diploma thesis. After measurements at this temperature, small optical changes on the surface of the MACOR plate at the top of the sample holder could be detected. Although repeated measurements at this temperature did not cause any observable change, it was decided not to increase the temperature in order to prevent potential damage of the sample holder. For future measurements, it is planned to test the absolute limit of the maximum temperature of the sample holder.

- **Expansion/modification for the measurement of thin films**: For potential technical application, thin films of a given sample are often more desired than bulk samples. In addition, the properties of thin films can significantly deviate from the respective bulk sample. To simultaneously measure the Seebeck- and Nernst coefficient of a thin film on an isolating substrate, modifications of the head of the sample holder and the sample contacts need to be considered.

- **Expansion for resistivity and Hall effect measurements**: For this diploma thesis, resistivity measurements for additional characterization of the sample were made using an ULVAC ZEM-3 device. However, the contact points for the Nernst effect measurements on top of the sample can easily be reused and expanded to implement the well known Van-der-Pauw method for resistivity and Hall effect measurements. The only required addition would be a device that can switch the connections from one of the nanovoltmeters to an AC resistance bridge device.

Acknowledgements

First, I want to thank my supervisor Ernst Bauer for his mentoring and support. He constantly showed interest in my diploma thesis and always provided valuable input.

Further, I want to thank Michael Parzer for his support and guidance. Our cooperation helped me gain a lot of knowledge, develop new skills and made the thesis a truly enjoyable experience for me.

In addition, I want to thank the Japan Science and Technology Agency (JST) programs MIRAI, JPMJMI19A1 for supporting the research of this diploma thesis.

Finally, I want to thank my family for their encouragement and unconditional support.

References

[1] M. Mizuguchi and S. Nakatsuji, "Energy-harvesting materials based on the anomalous nernst effect," *Science and technology of advanced materials*, vol. 20, no. 1, pp. 262–275, 2019.

[2] S. Memon, *Advanced Thermoelectric Materials for Energy Harvesting Applications*. BoD–Books on Demand, 2019.

[3] R. Gross and A. Marx, *Festkörperphysik*. Oldenbourg Wissenschaftsverlag, 2012.

[4] R. H. Tarkhanyan, "Magneto-seebeck and nernst effects in porous semiconductors with hierarchically distributed nano-to micro-scale pores," *Journal of Magnetism and Magnetic Materials*, vol. 519, p. 167444, 2021.

[5] W. Nernst, "Ueber die electromotorischen kräfte, welche durch den magnetismus in von einem wärmestrome durchflossenen metallplatten geweckt werden," *Annalen der Physik*, vol. 267, no. 8, pp. 760–789, 1887.

[6] M. Mizuguchi and S. Nakatsuji, "Energy-harvesting materials based on the anomalous nernst effect," *Science and Technology of Advanced Materials*, vol. 20, pp. 262–275, 03 2019.

[7] C. Fu, S. N. Guin, S. J. Watzman, G. Li, E. Liu, N. Kumar, V. Süβ, W. Schnelle, G. Auffermann, C. Shekhar, *et al.*, "Large nernst power factor over a broad temperature range in polycrystalline weyl semimetal nbp," *Energy & Environmental Science*, vol. 11, no. 10, pp. 2813–2820, 2018.

[8] Y. Sakuraba, K. Hyodo, A. Sakuma, and S. Mitani, "Giant anomalous nernst effect in the $Co_2MnAl_{1-x}Si_x$ heusler alloy induced by fermi level tuning and atomic ordering," *Phys. Rev. B*, vol. 101, p. 134407, Apr 2020.

[9] M. Ikhlas, T. Tomita, T. Koretsune, M.-T. Suzuki, D. Nishio-Hamane, R. Arita, Y. Otani, and S. Nakatsuji, "Large anomalous nernst effect at room temperature in a chiral antiferromagnet," *Nature Physics*, vol. 13, no. 11, pp. 1085–1090, 2017.

[10] B. A. Bernevig, C. Felser, and H. Beidenkopf, "Progress and prospects in magnetic topological materials," *Nature*, vol. 603, no. 7899, pp. 41–51, 2022.

[11] K. Behnia, *Fundamentals of thermoelectricity*. OUP Oxford, 2015.

[12] "Nist typer thermocouple reference data." https://srdata.nist.gov/its90/download/type_r.tab.

[13] A. Guan, H. Wang, H. Jin, W. Chu, Y. Guo, and G. Lu, "An experimental apparatus for simultaneously measuring seebeck coefficient and electrical resis-

tivity from 100 k to 600 k," *Review of Scientific Instruments*, vol. 84, no. 4, p. 043903, 2013.

[14] J. de Boor and E. Müller, "Data analysis for seebeck coefficient measurements," *Review of Scientific Instruments*, vol. 84, no. 6, p. 065102, 2013.

[15] "Ls 335 temperature controller." `https://www.corning.com/emea/de/products/advanced-optics/product-materials/specialty-glass-and-glass-ceramics/glass-ceramics/macor.html`.

[16] "Keithley 2182a." `https://www.tek.com/keithley-low-level-sensitive-and-specialty-instruments/keithley-nanovoltmeter-model-2182a`.

[17] "Ls 335 temperature controller." `https://www.lakeshore.com/products/categories/overview/temperature-products/cryogenic-temperature-controllers/model-335-cryogenic-temperature-controller`.

[18] "Struers accutom-100." `https://www.struers.com/de-DE/Products/Cutting/Cutting-equipment/Accutom`.

[19] "Ulvac zem 3." `https://www.ulvac.com/components/Thermal-Instruments/Thermoelectric-Testers/ZEM-3-Series`.

[20] "Constantan vdm metals." `https://www.vdm-metals.com/de/produkte-und-services/legierungen-und-halbzeuge/werkstoff-gesamtportfolio/#product=Korrosionsbest%C3%A4ndige%20Legierungen`.

[21] Z. Lu, N. D. Lowhorn, W. Wong-Ng, W. Zhang, E. L. Thomas, M. Otani, M. L. Green, T. N. Tran, C. Caylor, N. Dilley, *et al.*, "Statistical analysis of a round-robin measurement survey of two candidate materials for a seebeck coefficient standard reference material," *Journal of research of the National Institute of Standards and Technology*, vol. 114, no. 1, p. 37, 2009.

[22] N. Lowhorn, W. Wong-Ng, W. Zhang, Z. Lu, M. Otani, E. Thomas, M. Green, T. Tran, N. Dilley, S. Ghamaty, *et al.*, "Round-robin measurements of two candidate materials for a seebeck coefficient standard reference material™," *Applied Physics A*, vol. 94, no. 2, pp. 231–234, 2009.

[23] C. Gallo, B. Chandrasekhar, and P. Sutter, "Transport properties of bismuth single crystals," *Journal of Applied Physics*, vol. 34, no. 1, pp. 144–152, 1963.

[24] O. Prakash, A. Kumar, A. Thamizhavel, and S. Ramakrishnan, "Discovery of superconductivity in pure bi single crystal," *arXiv preprint arXiv:1603.04310*, 2016.

[25] K. Behnia, "The nernst effect and the boundaries of the fermi liquid picture," *Journal of Physics: Condensed Matter*, vol. 21, p. 113101, feb 2009.

[26] M. Hamabe, S. Yamamoto, S. Yamaguchi, H. Takahashi, H. Okumura, I. Yone-naga, T. Sasaki, and K. Watanabe, "Magnetic field effect for improvement of thermoelectric conversion: a proposal for nernst-seebeck element," in *Proceedings ICT'03. 22nd International Conference on Thermoelectrics (IEEE Cat. No. 03TH8726)*, pp. 567–570, IEEE, 2003.

[27] Y. Hasegawa, Y. Ishikawa, T. Saso, H. Shirai, H. Morita, T. Komine, and H. Nakamura, "A method for analysis of carrier density and mobility in poly-crystalline bismuth," *Physica B: Condensed Matter*, vol. 382, no. 1-2, pp. 140–146, 2006.

[28] T. Arisaka, M. Otsuka, and Y. Hasegawa, "Investigation of carrier scattering process in polycrystalline bulk bismuth at 300 k," *Journal of Applied Physics*, vol. 123, no. 23, p. 235107, 2018.

[29] S. Sharma and C. Yadav, "Experimental setup for the seebeck and nernst coefficient measurements," *Review of Scientific Instruments*, vol. 91, no. 12, p. 123907, 2020.

[30] J. de Sande and J. Guerra, "Nernst-ettingshausen effect in polycrystalline bismuth at high temperature," *Physical Review B*, vol. 45, no. 20, p. 11469, 1992.

[31] J.-P. Michenaud, E. Cheruvier, and J. Issi, "Field dependence of thermomagnetic effects in bismuth," *Solid State Communications*, vol. 9, no. 16, pp. 1433–1435, 1971.

[32] F. Spathelf, B. Fauqué, and K. Behnia, "Magneto-seebeck effect in bismuth," *arXiv preprint arXiv:2203.10069*, 2022.

[33] R. Hartman, "Temperature dependence of the low-field galvanomagnetic coefficients of bismuth," *Physical Review*, vol. 181, no. 3, p. 1070, 1969.

[34] K. Behnia, "On the origin and the amplitude of t-square resistivity in fermi liquids," *Annalen der Physik*, vol. 534, no. 5, p. 2100588, 2022.

[35] J.-P. Michenaud, E. Cheruvier, and J. Issi, "Field dependence of thermomagnetic effects in bismuth," *Solid State Communications*, vol. 9, no. 16, pp. 1433–1435, 1971.

[36] R. Y. Umetsu, K. Kobayashi, A. Fujita, R. Kainuma, and K. Ishida, "Phase stability and magnetic properties of l21 phase in co2mn (al1- xsix) heusler alloys," *Scripta Materialia*, vol. 58, no. 9, pp. 723–726, 2008.

[37] N. Kourov, V. Marchenkov, A. Korolev, L. Stashkova, S. Emel'yanova, and H. Weber, "Specific features of the properties of half-metallic ferromagnetic heusler alloys fe2mnal, fe2mnsi, and co2mnal," *Physics of the Solid State*, vol. 57, no. 4, pp. 700–708, 2015.

[38] F. Mende, J. Noky, S. N. Guin, G. H. Fecher, K. Manna, P. Adler, W. Schnelle, Y. Sun, C. Fu, and C. Felser, "Large anomalous hall and nernst effects in high curie-temperature iron-based heusler compounds," *Advanced Science*, vol. 8, no. 17, p. 2100782, 2021.

[39] T. Gasi, V. Ksenofontov, J. Kiss, S. Chadov, A. Nayak, M. Nicklas, J. Winterlik, M. Schwall, P. Klaer, P. Adler, *et al.*, "Iron-based heusler compounds fe 2 y z: Comparison with theoretical predictions of the crystal structure and magnetic properties," *Physical Review B*, vol. 87, no. 6, p. 064411, 2013.

[40] Y. Zhang, W. Wang, H. Zhang, E. Liu, R. Ma, and G. Wu, "Structure and magnetic properties of fe2niz (z= al, ga, si and ge) heusler alloys," *Physica B: Condensed Matter*, vol. 420, pp. 86–89, 2013.

[41] R. Ducher, R. Kainuma, and K. Ishida, "Phase equilibria in the ni–fe–ga alloy system," *Journal of alloys and compounds*, vol. 463, no. 1-2, pp. 213–219, 2008.

[42] A. Sakai, S. Minami, T. Koretsune, T. Chen, T. Higo, Y. Wang, T. Nomoto, M. Hirayama, S. Miwa, D. Nishio-Hamane, *et al.*, "Iron-based binary ferromagnets for transverse thermoelectric conversion," *Nature*, vol. 581, no. 7806, pp. 53–57, 2020.